

AFOSR-TR- 79 - 1259

Edward L. Ginzton Laboratory
W. W. Hansen Laboratories of Physics
Stanford University
Stanford, California

12
LEVEL

AD A 078088

6
ACOUSTIC MICROSCOPY FOR NONDESTRUCTIVE EVALUATION
OF MATERIALS

9 Semiannual Technical Report, 1 Feb - 31 Jul 79,

for the period

1 February - 31 July 1979

16 23061

17 B2

14 GL-3023

11 1979

Sponsored by
Advanced Research Projects Agency (DOD)
ARPA Order No. 3569

Monitored by NE Under Contract #~~44-0000-0000~~

15 F49628-78-C-0098

✓ ARPA Order-3569

12 85

The views and conclusions contained in this document are those of the authors and should not be interpreted as necessarily representing the official policies, either expressed or implied, of the Defense Advanced Research Projects Agency or the U.S. Government.

18 AFOSR

19 TR-79-1259

DDC

RECEIVED
DEC 12 1979

D

10
Principal Investigator: Professor C. F./Quate

G.L. Report No. 3023

Approved for public release;
distribution unlimited.

79 12 10 117

409 640

WUG FILE COPY

REPORT DOCUMENTATION PAGE		READ INSTRUCTIONS BEFORE COMPLETING FORM
1. REPORT NUMBER AFOSR-TR- 79 - 1259	2. GOVT ACCESSION NO.	3. RECIPIENT'S CATALOG NUMBER
4. TITLE (and Subtitle) ACOUSTIC MICROSCOPY FOR NONDESTRUCTIVE EVALUATION OF MATERIALS		5. TYPE OF REPORT & PERIOD COVERED Semiannual Technical Report 1 February - 31 July 1979
		6. PERFORMING ORG. REPORT NUMBER G.L. Report No. 30237
7. AUTHOR(s) C.F. Quate		8. CONTRACT OR GRANT NUMBER(s) F49620-78-C-0098 ¹⁰⁰
9. PERFORMING ORGANIZATION NAME AND ADDRESS Edward L. Ginzton Laboratory Stanford University Stanford, California 94305		10. PROGRAM ELEMENT, PROJECT, TASK AREA & WORK UNIT NUMBERS 2306/B2 0410 61102F 627128
11. CONTROLLING OFFICE NAME AND ADDRESS Advanced Research Projects Agency (DOD) 1400 Wilson Boulevard Arlington, Virginia 22209		12. REPORT DATE 1979
		13. NUMBER OF PAGES 84
14. MONITORING AGENCY NAME & ADDRESS (if different from Controlling Office) Air Force Office of Scientific Research /NE Bolling Air Force Base Washington, D.C. 20332		15. SECURITY CLASS. (of this report) UNCLASSIFIED
		15a. DECLASSIFICATION/DOWNGRADING SCHEDULE
16. DISTRIBUTION STATEMENT (of this Report) "Approved for public release; distribution unlimited"		
17. DISTRIBUTION STATEMENT (of the abstract entered in Block 20, if different from Report)		
18. SUPPLEMENTARY NOTES		
19. KEY WORDS (Continue on reverse side if necessary and identify by block number) Acoustic microscopy Focused laser beam Liquid gallium Radiated acoustic energy Computer plots Aberrations Photo acoustic imaging		
20. ABSTRACT (Continue on reverse side if necessary and identify by block number) The progress in our research in the field of acoustic microscopy is described for the first half of 1979. The properties and design of the acoustic transducer lens combination is detailed. The source of contact in the acoustic images for both material surfaces and integrated circuits is discussed with the view of determining how small changes in surface elastic properties alter the reflectivity for a spherically converging beam. The use of liquid gallium in the lens is described. Some of the work on the photoacoustic microscope is included.		

Unclassified

TABLE OF CONTENTS

	<u>Page</u>
I. INTRODUCTION AND SUMMARY.	1
II. TECHNICAL CONTENT	3
1. Material Studies.	3
2. Theoretical Considerations.	10
3. Acoustic Components	11
A. Introduction.	11
B. Diffraction	12
C. Beam Steering and Top Dot Alignment	18
D. Transducer Design and Evaluation.	23
E. Acoustic Matching Layers.	42
F. Lens Design	55
References for Section 3.	66
4. Photoacoustics.	68
5. Imaging with High Velocity Liquids Metals - Gallium . . .	70
III. ADDITIONAL ACTIVITIES	81

Accession For	
NTIS GRA&I	<input checked="" type="checkbox"/>
DDC TAB	<input type="checkbox"/>
Unannounced	<input type="checkbox"/>
Justification	
By	
Distribution/	
Availability Codes	
Dist	Availand/or special
A	

AIR FORCE OFFICE OF SCIENTIFIC RESEARCH (AFSC)
 NOTICE OF TRANSMITTAL TO DDC
 This technical report has been reviewed and is
 approved for public release in accordance with AFM 190-12 (7b).
 Distribution is unlimited.
 A. D. BLOSE
 Technical Information Officer

I. INTRODUCTION AND SUMMARY

During this interval we made several advances and consolidated our understanding of the acoustic microscope. It is now possible to image small changes in the elastic properties of a surface with good contrast. We have gained more insight into the source of this contrast and why it is increased as the spacing between the lens and the object is varied. This is a feature unique to acoustic microscopy and the technique reveals more and more as we continue with the study. The experimental results presented here in Section II will be analyzed in the coming months with computer plots pertaining to the actual object now under study. We have done additional work on the lens design for it is the key element in the microscope. We are receiving an increasing number of inquiries from others intending to enter this field and it is the detailed understanding of the lens design that is their first interest. The work presented in this report is a full treatment of that problem. We have continued our work on photoacoustic imaging. There we heat the sample under study with a focused laser beam modulated in amplitude with a frequency in the microwave range. The radiated acoustic energy is picked up with our standard acoustic lens and the object is scanned to form the image.

Perhaps the most significant advance made during this interval is described in the last Section (II.5). We are now able to penetrate the liquid solid interface and focus the beam to a diffracted limited waist deep inside the solid. To achieve this we use liquid gallium with a rather high velocity for longitudinal waves ($\sim 3 \times 10^5$ cm/sec). At the liquid-solid interface we convert to shear waves and for those materials such as SiO_2 where the shear

wave velocity is less than the wave velocity in gallium we have found that aberrations can be suppressed to a degree where they are no longer troublesome. Under these conditions the diameter of the beam at the waist which is located inside the solid is less than the wavelength of shear waves. This point is important for the wavelength of shear waves is almost a factor of two less than that of longitudinal waves. Thus the mode conversion at the liquid-solid interface has two advantages, (1) it reduces the aberrations and (2) it provides us with a shorter wavelength in the solid.

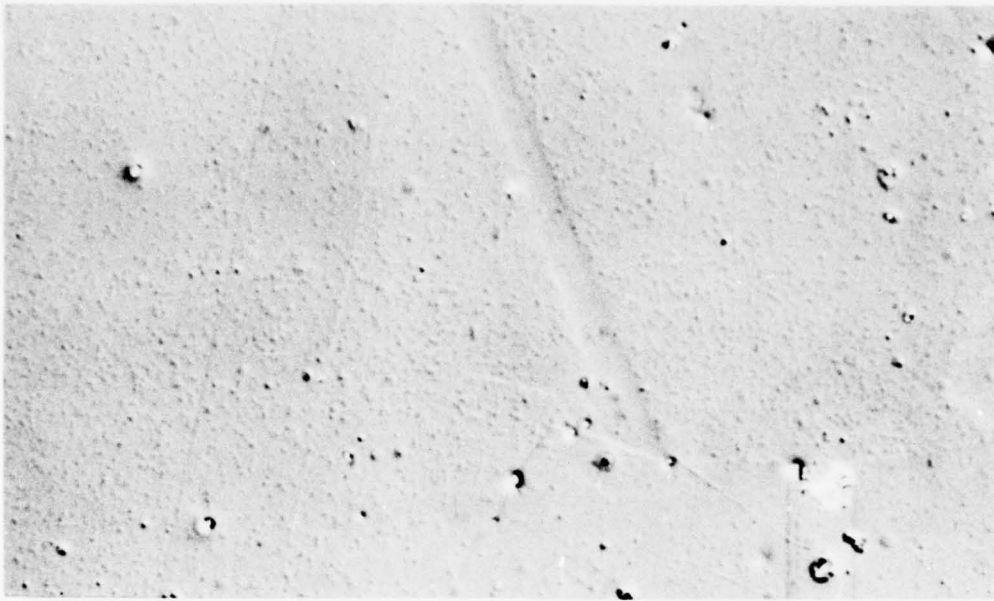
II. TECHNICAL CONTENT

1. Material Studies

Our work on material studies was reported at the ARPA/AFML Review of Progress in Quantitative NDE Conference held in La Jolla, California in July. Here we review those results and in addition we will include the recent work that gives us new insight into the defects of the silicon-on-sapphire devices that we introduced in our last report.

The material — α -brass — has proven to be interesting for this study since its elastic properties are anisotropic and this anisotropy can show up in the acoustic micrographs. The example that we have chosen is shown in Fig. 2.1. The polished surface as it appears in reflection in the optical instrument is shown in the upper figure. The grain boundary (lower right) is evident in this image as well as the straight edges of the twins. However, there is little contrast in the image and what there is comes from the residual surface contours that result from dissimilar polishing rates. The field of view in this image is $55 \times 90 \mu\text{m}$.

In the lower figure we show the same field as it appears with reflected acoustic waves (2500 MHz). The grain boundary (lower right) is clearly delineated since there is large contrast between the two grains. We attribute this to the difference in elastic constants that result from the different orientation of the two grains. The twins also show up in the acoustic micrograph with excellent contrast. In fact the boundary that shows up as the diagonal line in the upper right of the acoustic micrograph is so faint in the optical image that it is easily missed. In fact in the first optical images it was not seen. We had to return to the optical instrument and knowing where to look we were able to adjust the focus to find it.



(a)



(b)

FIG. 2-1. Optical (a) and acoustic (b) comparison of polished brass surface. Field of view is $55 \times 90 \mu\text{m}$.

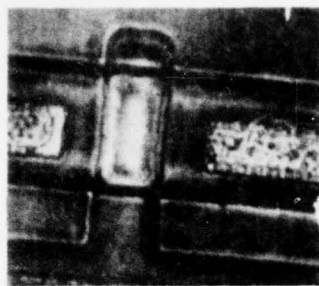
A second material has also proven to be most interesting in this study — namely, an alloy of Cobalt-Titanium. The material was polished and carefully studied with the optical microscope. The optical reflectivity was fairly uniform over the surface; the surface contours which result from nonuniform polishing rates were, of course, visible in the optical micrographs.

In the acoustic micrographs all of the features apparent in the optical images show up with high contrast in the acoustic reflectivity. The important point that we want to emphasize here is that we found additional information in the acoustic micrographs. They were bright points that appeared with increased acoustic reflection. Thus these regions of enhanced acoustic reflectivity represented regions where the elastic properties were distinctly different from the surrounding areas. The optical micrographs were uniform and revealed nothing in the way of detail in these particular points. We were able to prove all of this when we chemically etched this surface and found pits in the etched surface at each point where we found the bright spots in the acoustic micrographs. From this we conclude that these areas represented either 1) small voids beneath the surface, or 2) small regions with excess oxygen content which is known to increase the rate of etching. In either event we feel that it is an important step in demonstrating the power of acoustic microscopy in material studies. The full details of this study will be included in the proceedings of the 1979 ARPA/AFML Review of Progress in Quantitative NDE Conference held in La Jolla in July.

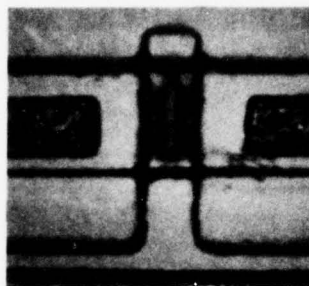
We will now return to the silicon-on-sapphire devices that were introduced in the last report. There we described our work with field effect transistors (SOS) as furnished to us by Bill Ham of the RCA Laboratories.

The study was limited to the gate region of these transistors and we were attempting to distinguish those gates that were defective. The defective gates exhibited high leakage current from source to drain when the gate was reversed biased. There were indeed differences in the acoustic images but a suitable criteria for distinguishing the defective gates were hard to establish.

We recall from the previous report that the acoustic information can be presented in two forms; first a normal micrograph of the surface which we record with an x-y scan in the lateral plane with a constant distance between the lens and the sample; second, a single line scan in the x-direction as compiled with various values of lens sample spacing. This gives information on the elastic properties beneath the surface. An illustration of these two forms of imaging is given in Fig. 17 of the last report (G.L. 2956). Figure 2.2 includes similar images for a second device (device B). The six micrographs (a - f) each for a different focal position show how the appearance of the gate changes with this variation. We want to concentrate our attention on the last figure (g). This is the x-z scan which is not an image but rather a presentation of the variation in a single line scan as the focal position is changed. We see that the horizontal line marked 'a' corresponds to the same focal position as does the image in the upper left marked (a). The gate region is marked at the top of (g) with the double arrows. In Fig. 2.3 we have assembled the x-z scans for 10 different gates on the SOS wafer. Each of these has been characterized with electrical measurements at the RCA Laboratories and it is known devices in (a) and in (b) are defective. The important point is that these two devices can be easily distinguished by a casual untrained observer from the remaining eight (which are all good). The



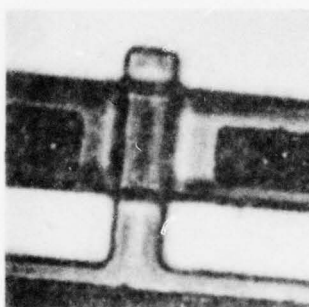
(a)



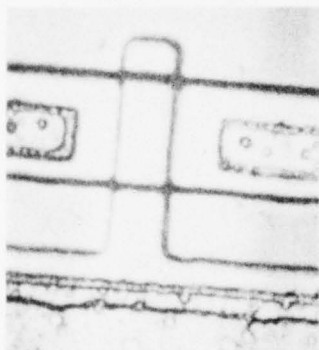
(d)



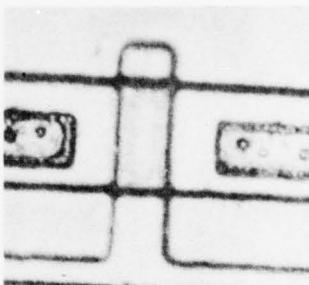
(b)



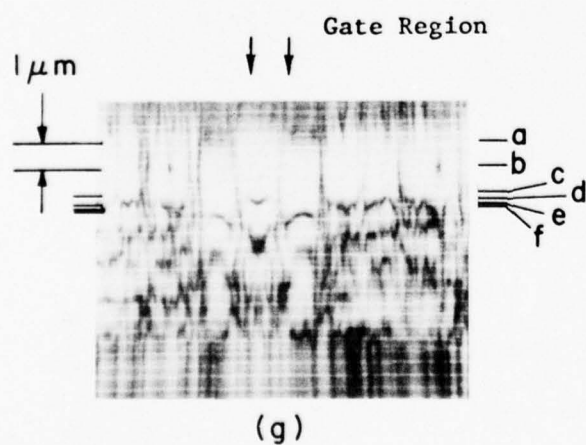
(e)



(c)



(f)



(g)

DEVICE B

FIG. 2-2. Acoustic micrographs for a high leakage FET at 6 focal planes (a) - (f). In (g), the $V(x,z)$ response is shown.

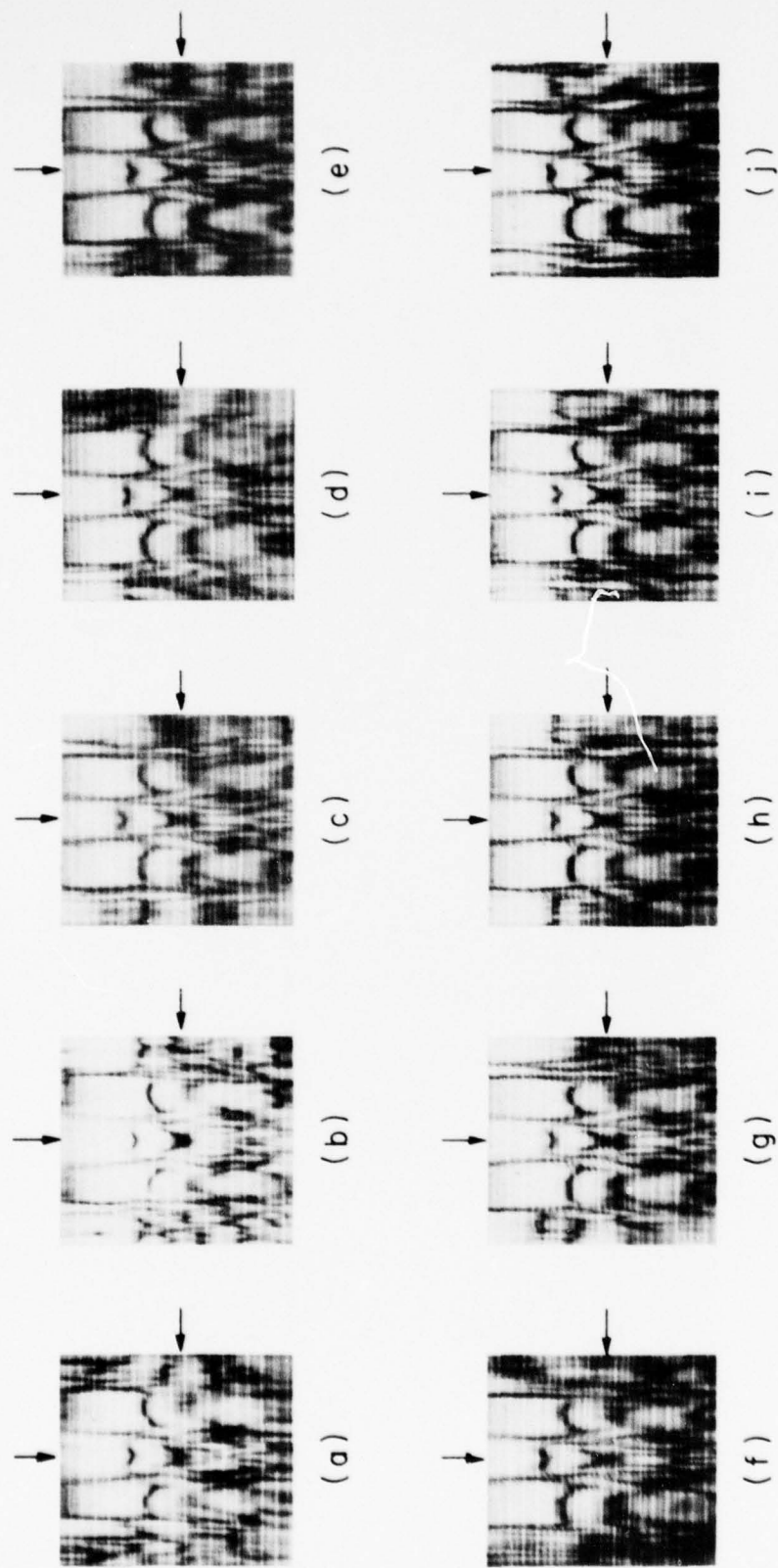


FIG. 2-3. $V(x,z)$ response for 10 different gates. Devices a and b exhibit high leakage current while c-j are good devices.

feature is in the gate region (marked by the arrow at the top) about midway down the figure (marked by the horizontal arrow on the right). We see the vertical extent of the blackened region within the gate is much less for the two defective gates than it is for the good devices.

We don't yet understand the full meaning of these differences but we are now in a position to build a theory for acoustic reflection from layered structures and this theory should permit us to explain these observed differences.

2. Theoretical Considerations

Our theoretical effort has been devoted to the two problems that were defined by the experimental observations recorded above: 1) the buried inclusions in the Co-Ti alloy, and 2) the elastic inhomogeneities in the layered structures in the region of the transistor gate.

For the study of the buried inclusion we have modeled this, as a first step, in the form of spherical cavity located just beneath the liquid-solid surface. We have, to date, set up the computer program for calculating the scattering coefficients for this cavity and we are now proceeding to incorporate this into our theory for the behavior of acoustic waves in the acoustic microscope. We will in time be able to calculate the response of the transducer as the focused beam is scanned across the buried cavity and correlate this with our measured values.

In the second problem we are confident that we can calculate the reflectivity from each of the various layered regions that make up the transistor and correlate this with the variations in the line scan that we have now measured. Much of this work is in hand for we have previously solved different parts of the problem. But we were sidetracked in this work for a period. We thought that the evidence indicated the problem with defective gates to be at either edge of the gate. The calculation of the acoustic reflectivity when the beam is covering the edge of the gate is very difficult. The evidence, as in Fig. 2.3 now indicates that the elastic inhomogeneities in the central region of the gate may be the source of the problem. This region is much easier to treat in a theoretical model and that is what we are now setting out to do.

3. Acoustic Components

A. Introduction

The critical component in our version of the acoustic microscope is of course the lens-transducer combination. We have been asked with increasing frequency about the details of this design and in this section we want to record these details. The work has extended over a number of months but was completed during the interval of this report. The lens design with its associated theory and the techniques for putting it all together, was crucial to the realization of our high resolution instrument operating near 3 GHz.

3. B. Diffraction

The complex distribution of the acoustic field amplitude at the back focal plane of the acoustic lens will affect the resolution performance of the acoustic lens as was outlined in the previous chapter. It is possible to increase the high spatial frequency response of the acoustic lens by illuminating the outer regions of the acoustic lens more strongly than the central regions, but the price for this is higher side-lobe levels in the focal plane beam response. These apodization schemes are difficult to accurately implement, and in general, a relatively uniform back focal plane distribution is desirable. Due to diffraction effects within the lens element it is not possible to uniformly illuminate the lens without having a significant portion of the acoustic energy fall outside the aperture of the lens. In order to understand the imaging properties of the acoustic lens and to minimize the loss of acoustic power, the diffraction within the lens element must be understood so that the lens and transducer can be properly designed. The effects of this diffraction are also of importance in calculating the efficiency of the piezoelectric transducers that are used to illuminate the lens. These effects will be considered more fully in Section D of this chapter.

The diffraction of sound in isotropic media has been considered by several authors for various geometries. In particular, Zemanek^{3.1} has calculated results for piston radiators as a function of distance from the radiator. The basic geometry considered is shown in Fig. 3.1. In his analysis Zemanek treated the diameter of the radiator normalized by the acoustic wavelength as a variable parameter. Atalar^{3.2}

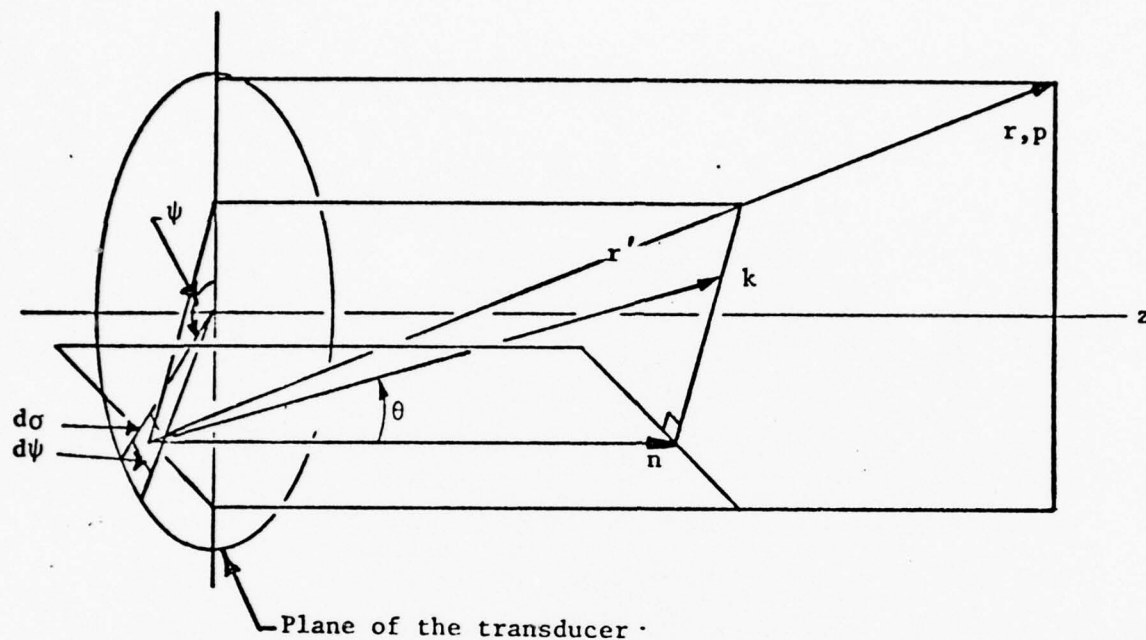


FIG. 3.1--Geometry for diffraction calculations. For the isotropic case the wave vector k and the power flow direction will be collinear.

applied an improved version of Zemanek's computational algorithm to the case of the acoustic lens, but an isotropic media was assumed. In this section the theory of Waterman^{3.3} and Papadakis^{3.4,3.5,3.6} is utilized to account for the crystalline anisotropy of sapphire.

For the geometry shown in Fig. 3.1 and considering an isotropic media (i.e., wavevector and energy flow are collinear), the acoustic field at a plane a distance z from the transducer is given by;^(3.1)

$$P(z,r) = \frac{j\rho ck_o}{2\pi} U_o \int_0^{R_t} \sigma d\sigma \int_0^{2\pi} \frac{e^{j(\omega t - k_o r')}}{r'} d\psi \quad (3.1)$$

where $j = (-1)^{1/2}$, U_o is the peak amplitude of the transducer particle velocity, ρ is the density, c is the velocity of sound, $k_o = 2\pi/\lambda$ is the wavevector, λ is the acoustic wavelength, R_t is the radius of the transducer, ω is the frequency of operation, t is the time and r' is the distance from a point on the transducer (σ, ψ) to the field point of interest (z, r) . The distance r' is given by

$$r' = (r^2 + \sigma^2 - 2r\sigma \sin \theta \cos \psi)^{1/2} \quad (3.2)$$

where all the quantities are shown in Fig. 3.1. Thus the field at a given point $P(z, r)$ is found by breaking the transducer into a large number of infinitesimal sections and summing the contribution of each. This technique is adequate when the wave vector and the energy flow are in the same direction as for an isotropic medium. This condition will not be met for arbitrary directions in anisotropic media, and

therefore one must consider the deviation between power flow and wavevector as a function of the crystalline direction in order to calculate the acoustic field at arbitrary planes in front of the transducer. For non-symmetry directions in an anisotropic media this calculation would be quite tedious. Fortunately the case considered here is simplified by the fact that propagation is along the c-axis (6-fold axis of symmetry) of a hexagonal crystal.

It has been shown by Papadakis^{3.6} based on work by Waterman,^{3.3} that for propagation along a principle axis Eq. (3.2) can be modified to;

$$P(z,r) = \frac{j\rho c k_o}{2\pi} U_o \int_0^{R_t} \sigma d\sigma \int_0^{2\pi} \frac{e^{j[\omega t - k_o |r'| (1 + b(1 - 2b)\theta^2)]}}{r'} d\psi . \quad (3.3)$$

Thus the anisotropy can be approximated by incorporating a shift within the phase term of each infinitesimal radiator. This is accomplished by adding an angular dependence to the wave vector [i.e., $k = k_o (1 + b(1 - 2b)\theta^2)$]. The proportionality constant is $b(1 - 2b)$ where b is a measure for anisotropy in the crystal and is given by Waterman^{3.3} as,

$$b = \frac{(c_{33} - c_{13} - 2c_{44})(c_{33} + c_{13})}{2c_{33}(c_{33} - c_{44})} \quad (3.4)$$

for near c-axis propagation in a hexagonal crystal. The c_{ij} 's in the above are the elastic constants of the material and for sapphire $b = 0.1612$. The validity of the approximation of Eq. (3.3) will depend on how well the parabolic phase shift models the anisotropy of

the crystal as a function of the angular deviation from the c-axis. For the geometry considered here this angular deviation will be small (less than 10 degrees) and thus the approximation should be valid.

A computer program was written to calculate the acoustic field at various distances for both the anisotropic and isotropic cases. This program is only a slightly modified version of a program developed by Atalar^{3.2} for the isotropic case. Calculated results for a frequency of 1 GHz with $R_t = 105 \mu\text{m}$ and $z = 2 \text{ mm}$ are shown in Fig. 3.2. The result based on an isotropic assumption is also shown (normalized to the same center value). For the isotropic case it can be seen that the 3 dB point of the acoustic field intensity is at a radius that is only 25% of the radius of the transducer. This "self-focusing" effect was observed by Zemanek to occur at a distance of one Fresnel length (R_t^2/λ) from the transducer which is applicable for this calculation. When the anisotropy of the crystal is included this "self-focusing" effect is greatly reduced. This is exactly what one would predict for sapphire by studying its slowness surface. Energy is guided preferentially along the c-axis and thus the effects of diffraction are reduced. Also shown in Fig. 3.2 is the phase of the acoustic field at the plane of interest. The phase change is important to the lens response if it is large (greater than a few radians) or irregular, but the phase changes for the cases here are not significant.

The above analysis can be used to pick the appropriate transducer size and crystal length to insure that the back focal plane of the lens will be properly illuminated. In general the crystal length and top

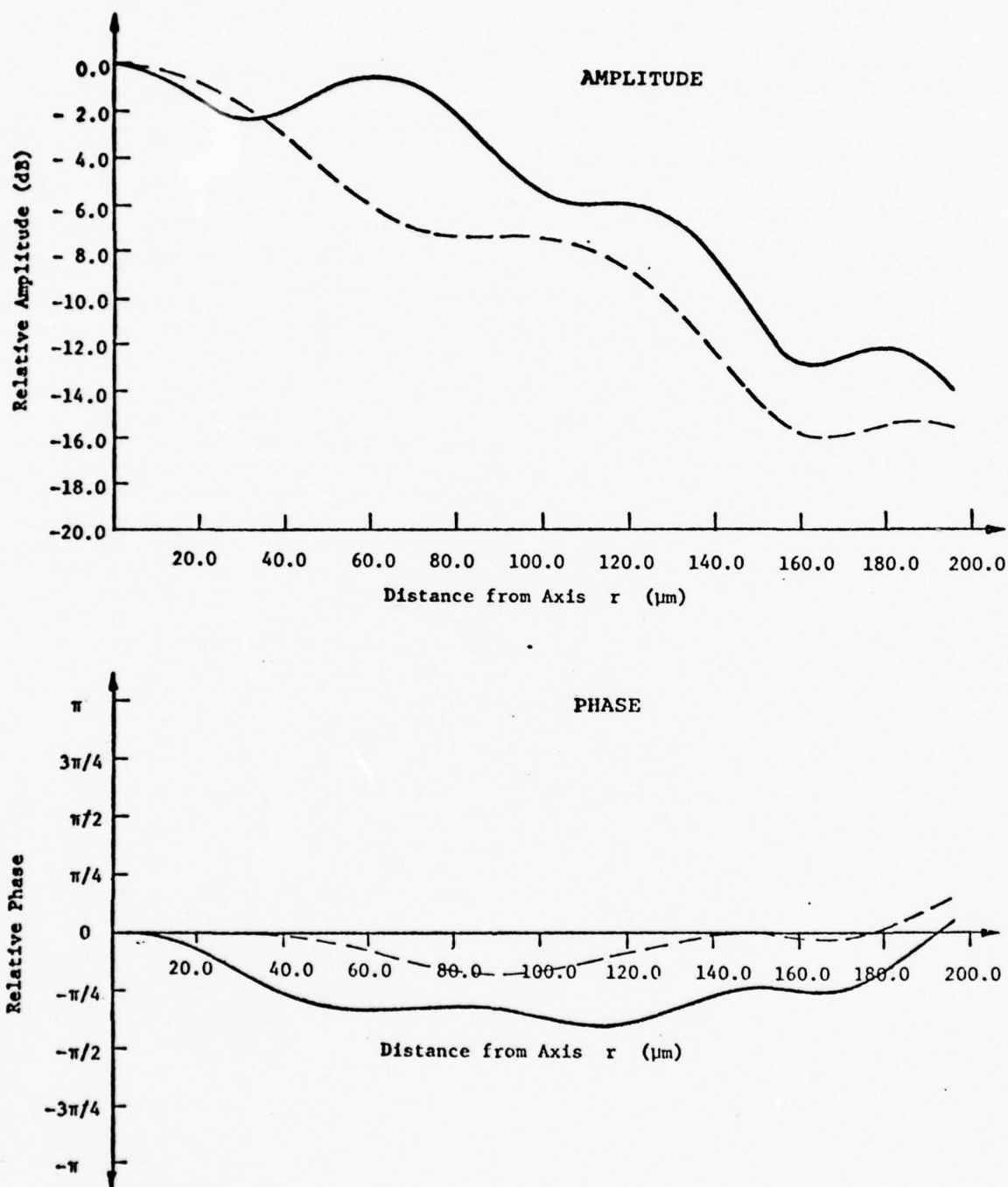


FIG. 3.2--Comparison between diffraction calculation for an anisotropic (solid line) and an isotropic (dashed line) solid. The calculation is for $R_t = 150 \mu\text{m}$, $z = 2000 \mu\text{m}$, $\lambda = 11.1 \mu\text{m}$ and $R_t^2/\lambda = 2027 \mu\text{m}$.

dot radius will be selected such that at the frequency of operation the lens will be 1 to 4 Fresnel lengths from the transducer. By keeping the crystal length at least 1 Fresnel length long it insures a smooth phase distribution at the lens. Also, by keeping the length from being much greater than 1 Fresnel length it allows one to work with a relatively large transducer radius as compared to the lens aperture. This proves convenient for fabrication purposes, especially for the small aperture acoustic lenses where it is desired to illuminate a circle of 30 μm radius or less.

C. Beam Steering and Top Dot Alignment

It has been implicit in the preceding calculations that the c-axis of the sapphire is accurately aligned with the geometric axis of the acoustic lens. If this is not the case anisotropy will cause the acoustic beam to be displaced from its geometric shadow as depicted in Fig. 3.3. If this displacement is on the order of the lens aperture then the illumination of the lens will be severely asymmetrical.

For propagation near the c-axis the amount of beam steering ϕ will be proportional to the angle between the geometric axis and the crystalline c-axis. If this misalignment of the two axes is θ , then it has been shown^{3.3} for propagation near the c-axis of a hexagonal crystal that;

$$\phi = \frac{(c_{13} + c_{33})(2c_{44} - c_{33} + c_{13})}{c_{33}(c_{33} - c_{44})} \theta \quad (3.5)$$

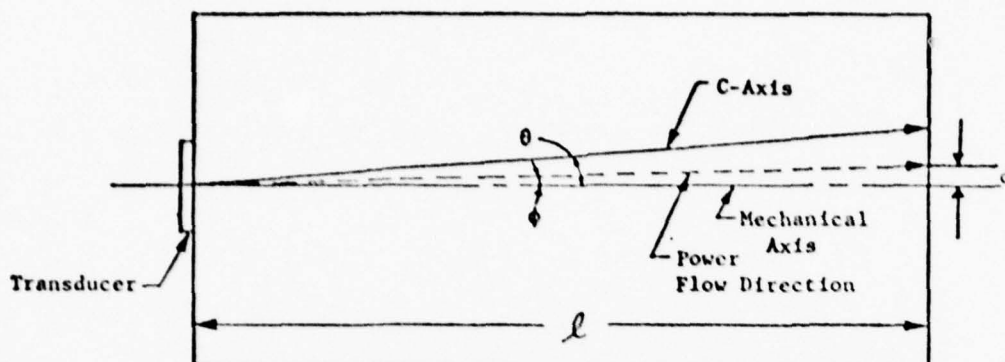


FIG. 3.3--Beam steering geometry.

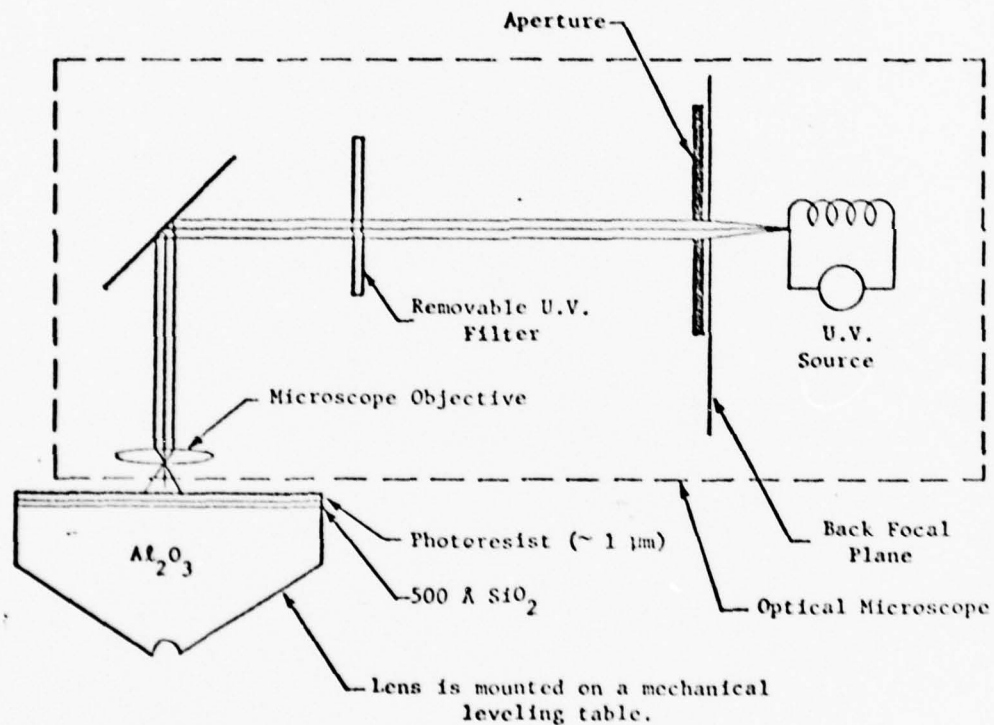


FIG. 3.4--Schematic of projection photolithography system used for top dot definition.

where c_{13} , c_{33} and c_{44} are the appropriate elastic constants for the material. For sapphire it is found that $\phi = 0.322 \theta$ for small values of θ . Consequently the beam displacement for a crystal of length ℓ will be;

$$d = \ell \tan (0.322\theta) . \quad (3.6)$$

Thus if θ is one degree and ℓ is 2 mm then d will be 11.2 μm . This much beam displacement can be a substantial fraction of the lens aperture and would result in back focal plane asymmetry. In order to minimize this effect the sapphire used is required to have its c-axis accurately aligned with the geometric axis of the lens. This alignment can be measured using x-ray techniques and the sapphire is not utilized unless this alignment error is less than 0.5 degrees. Thus, in worst cases, the error for a 2 mm long crystal would be less than 6 μm .

Even if the c-axis is perfectly aligned it is still difficult to ensure that the lens will be symmetrically illuminated. With large lenses where misalignments of 25 μm or less are tolerable, it is possible to use mechanical masking techniques to center the piezo-electric transducer with respect to the lens. However, with lens apertures of 50 μm or less this error is not acceptable. In order to minimize the mechanical alignment problem an optical technique was developed. Before starting the transducer fabrication a thin ($\sim 500 \text{ \AA}$) silicon dioxide layer is deposited on the back surface of the acoustic lens. Using a projection photolithographic technique that is described below, a hole is cut in this oxide that is mechanically centered directly

above the lens and is of the appropriate diameter for the transducer. The transducer is then fabricated by evaporating and sputtering the appropriate materials over this hole. The rim of this hole is used in the final step to define the top dot for the transducer.

A schematic diagram of the projection photolithographic system is shown in Fig. 3.4. The lens with the SiO_2 layer plus a layer of photoresist is placed in the optical microscope which has an ultra-violet filter in the optical path to prevent premature exposure of the photoresist. The lens is mechanically adjusted such that the back surface of the acoustic lens is perpendicular to the optical axis of the microscope. This is accomplished by focusing the microscope on the back surface of the lens and adjusting the tilt such that it is in focus over the entire surface. This insures that the alignment between the optical axis of the microscope and the mechanical axis of the lens is no worse than 0.05 degrees for most cases. The acoustic lens is then moved toward the optical lens until the front surface of the acoustic lens comes into focus. An aperture of the appropriate size is placed in the back focal plane of the microscope and is projected as a spot of light that can be centered about the rim of the acoustic lens. When this centering has been accurately accomplished, the acoustic lens is translated vertically away from the optical lens until the light spot comes into focus on the back surface of the acoustic lens. If the motion of the acoustic lens is truly vertical, then the spot of light is directly above the spherical cavity that forms the acoustic lens. At this point the UV filter can be removed and the light intensity can

be increased in order to expose the desired region of the photoresist. Then, using standard photolithographic techniques, a hole can be cut in the SiO_2 at the desired location. Using this technique it is possible to get the top dot mechanically aligned to within 2 μm .

The worst case beam misalignment of 8 μm (mechanical plus beam steering) is tolerable for lens sizes presently being used, but for lenses with a radius of less than 20 μm it will be excessive. The major factor contributing to this error is beam steering, and consequently, it is desirable to use a material for the lens that would reduce this problem. The most obvious solution would be to put a tighter constraint on the c-axis alignment of the sapphire, but it becomes difficult to verify its alignment and expensive to obtain. A second solution is to use a material other than sapphire that has a reduced beam steering effect. Any new material must also have a high longitudinal acoustic velocity in order to keep spherical aberrations to a minimum. A good candidate material is yttrium aluminum garnet (YAG) which has cubic symmetry. YAG is a mechanically strong material and thus not subject to scratching or chipping, and its longitudinal acoustic velocity of 8.56 km/sec is large enough so that spherical aberration effects will still be low. For a cubic crystal with propagation along the [001] crystalline axis, it has been shown^{3,3} that the beam steering angle is given by;

$$\phi = \frac{(c_{11} + c_{12})(c_{11} - c_{12} - 2c_{44})}{c_{11}(c_{44} - c_{11})} \theta \quad (3.7)$$

where c_{11} , c_{12} and c_{44} are the appropriate elastic constants. For

YAG the result is $\phi = 0.0449\theta$ and thus the effects of beam steering due to crystalline anisotropy are only 14% as large as for sapphire. Thus by comparison the worst case beam steering error would be reduced from 6 μm to less than 1 μm .

D. Transducer Design and Evaluation

In order to maintain as much dynamic range as possible in the acoustic microscope, high efficiency piezoelectric transducers are needed to launch the acoustic wave that illuminates the lens and to receive the weak return that comes from the object that is being scanned. The microscope has been operated at acoustic frequencies from a few hundred megahertz to frequencies above 3.0 gigahertz. In these frequency ranges a thin film piezoelectric transducer structure where the films are grown by evaporation, sputtering or some other thin film technology is desirable due to the relative ease of fabrication. Since high conversion efficiency and large bandwidth are desired, a piezoelectric material with a large piezoelectric coupling constant is needed. This material must also lend itself to thin film processing techniques. ZnO is chosen as the piezoelectric material since it most successfully meets all the above criterion. The design of these transducers is based on the theoretical model described in a review article by Reeder and Winslow.^{3,7} A comparison between theoretical and experimental results as a function of frequency is given for some representative transducers. The effects of acoustic diffraction and attenuation within the sapphire are included within the model. A two-element matching network is described that can be used to tune the

transducers at frequencies above 3 GHz with good bandwidth. The theoretical response of these transducers is given for various values of the matching elements.

The basic geometry for the piezoelectric transducer considered here is shown in Fig. 3.5. In this figure the t_i 's represent thicknesses, v_i 's longitudinal velocities and z_i 's mechanical impedances where $i = 0, 1, 2$ and d refer to the layers shown. This is identical to the geometry considered by Reeder and Winslow except for the bond wire which is included here in recognition of the physical reality that electrical connection must be made to the top electrode. The operation of this device is straightforward. A high frequency electromagnetic field is applied across the piezoelectric material through electrical connections to the two metal electrodes that sandwich it. This causes the piezoelectric material to expand and contract in response to the polarity of the electric field, which in turn excites an acoustic wave that propagates into the substrate material. The strength of this wave is dependent on the thickness of the various layers and their mechanical properties. The goal of this device, of course, is to convert as much of the incident electromagnetic energy into acoustic energy as possible. To do this a resonant structure is employed, i.e., the piezoelectric layer thickness is chosen such that its response is a maximum at the desired frequency of operation.

In order to analyze the geometry of Fig. 3.5, several simplifying assumptions are made. The transducer is taken to be one dimensional, i.e., the diameter of the transducer is much greater than an acoustic

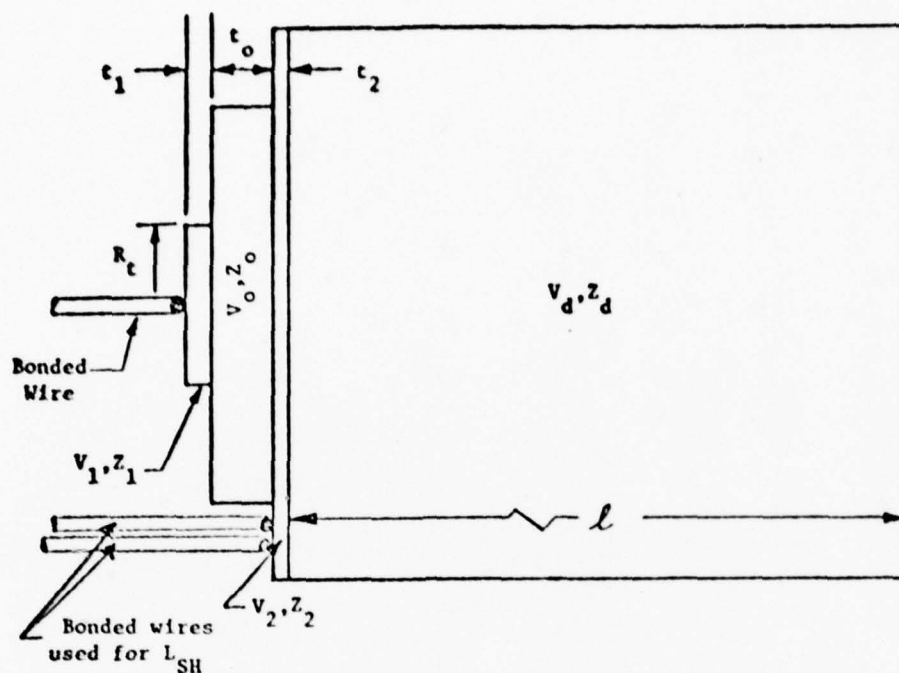


FIG. 3.5--Geometry of piezoelectric transducers. V_i 's are longitudinal acoustic velocities, Z_i 's are mechanical impedances and t_i 's are the layer thicknesses. Typically an Au-ZnO-Au- Al_2O_3 geometry is used.

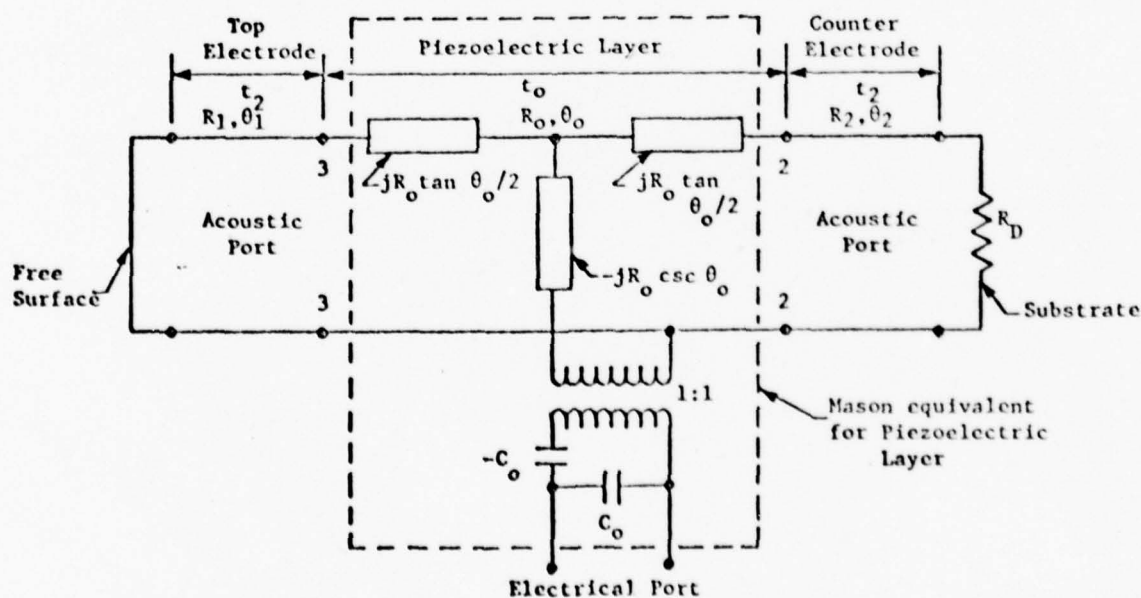


FIG. 3.6--Electrical equivalent circuit for the geometry of Fig. 3.5.

wavelength and thus both acoustic and electromagnetic fields are considered to vary only in the thickness direction. The thin layered structures are assumed to be acoustically lossless and the top electrode is approximated as a free surface. Finally, the orientation of the piezoelectric film and the substrate are taken to be such that only the longitudinal acoustic mode will be excited. Based on the above assumptions it has been found^{3.7-3.10} that the geometry of Fig. 3.5 can be modeled by the electrical equivalent circuit shown in Fig. 3.6. The region delineated by the dashed line is the familiar Mason equivalent circuit^{3.8} for the piezoelectric region. The Mason model is found by first finding a general solution for the acoustic and electric fields within the piezoelectric material^{3.8,3.9} and then matching these fields to the three-port terminal variables imposed. The three ports of the device consist of the electrical port and two acoustic ports that exist on either side of the piezoelectric film. The procedure given results in a set of three simultaneous equations relating the input voltage and mechanical force to the output current and acoustic particle velocity. These simultaneous equations are identical to the ones that are found by writing the terminal equations for the Mason model.

The model of Fig. 3.6 is completed by representing the top and bottom electrodes as transmission lines^{3.10} whose lengths are determined by the layer thickness and whose characteristic impedances are determined by the mechanical impedance of the electrode material. The top surface is assumed to be adequately represented as a free surface and as such, is represented by an acoustic short circuit while the substrate material is represented as a real impedance load whose value is

determined by the mechanical impedance of the substrate. Representing the substrate as a real impedance implies that its acoustic length is long compared to the time duration of any input signal that will be used during operation or testing of the device.

In order to make the physical connection between the Mason model of Fig. 3.6 and the piezoelectric transducer, it is necessary to relate the electrical component values to the mechanical properties of the device. The following definitions are used for the parameters of the Mason model:

$C_o = \frac{\epsilon A}{t_o}$ is the clamped static capacitance of the transducer where A is the transducer area, ϵ is the effective dielectric constant of the piezoelectric material and t_o is the thickness of the piezoelectric layer,

$f_o = \frac{V_o}{2t_o}$ is the frequency at which the piezoelectric layer is half an acoustic wavelength thick,

$\theta_o = \pi f / f_o$ is the acoustic length of the piezoelectric layer at a frequency f ,

$\phi = hC_o$ can be regarded as the turns ratio of an acoustic to electric transformer where h is the appropriate piezoelectric constant for the material, and

$R_o = \frac{Az_o}{\phi^2} = \frac{\pi}{\omega_o C_o k_t^2}$ is the electrical ohms equivalent of the mechanical impedance of the piezoelectric

layer where A is the area of the transducer,
 z_o is the mechanical impedance of the layer,
 $\omega_o = 2\pi f_o$ and k_t is the piezoelectric coupling
constant for the film.

Since the piezoelectric layer is of central importance to the
analysis of the transducer, it is convenient to define the following
normalized parameters;

$d_1 = V_o t_1 / V_1 t_o$ is the normalized thickness of the top elec-
trode,

$d_2 = V_o t_2 / V_2 t_o$ is the normalized thickness of the counter
electrode,

$r_1 = z_1 / z_o$ is the normalized acoustic impedance of the
top electrode,

$r_2 = z_2 / z_o$ is the normalized acoustic impedance of the
counter electrode and

$r_d = z_d / z_o$ is the normalized acoustic impedance of the
substrate.

The above parameters along with the piezoelectric coupling constant k_t ,
the static capacitance C_o and the half wavelength frequency f_o are
sufficient to completely describe the operation of the transducer
structure of Fig. 3.5.

The following set of equations can be written for the Mason equiva-
lent circuit contained in Fig. 3.6.

$$\begin{bmatrix} V_1 \\ V_2 \\ V_3 \end{bmatrix} = -j \begin{bmatrix} R_o \cot \theta_o & R_o \csc \theta_o & 1/\omega C_o \\ R_o \csc \theta_o & R_o \cot \theta_o & 1/\omega C_o \\ 1/\omega C_o & 1/\omega C_o & 1/\omega C_o \end{bmatrix} \begin{bmatrix} I_1 \\ I_2 \\ I_3 \end{bmatrix} \quad (3.8)$$

The impedances seen at the two acoustic ports can be easily found by applying lossless transmission line theory to the geometry of Fig. 3.6 and are given by;

$$z_1 = -\frac{V_1/I_2}{R_o} = jr_1 \tan \theta_1 \quad (3.9)$$

and

$$z_2 = -\frac{V_2/I_2}{R_o} = r_2 \frac{r_d \cos \theta_2 + jr_2 \sin \theta_2}{r_2 \cos \theta_2 + jr_d \sin \theta_2} \quad (3.10)$$

where $\theta_1 = \pi d_1 f / f_o$ and $\theta_2 = \pi d_2 f / f_o$ are the acoustic lengths of the respective layers. Simultaneous solution of Eqs. (3.8) - (3.10) for the input impedance at the electrical port gives;

$$z_3 = V_3/I_3 = \frac{1}{j\omega C_o} + \frac{P(f)}{R_o (\omega C_o)^2} \quad (3.11)$$

where

$$P(f) = \frac{2j(1 - \cos \theta_o) + (z_1 + z_2) \sin \theta_o}{(1 + z_1 z_2) \sin \theta_o - j(z_1 + z_2) \cos \theta_o} \quad (3.12)$$

By considering the real and imaginary parts of $P(f)/R_o (\omega C_o)^2$ to

represent the real and imaginary parts of the acoustic impedance of the transducer, it is possible to draw a simplified equivalent circuit of the transducer as shown within the dashed region of Fig. 3.7. The real part of the impedance R_a is known as the acoustic radiation resistance, while the imaginary part X_a represents a reactive term. The capacitor C_o is the static clamped capacitance of the transducer and is shown independent of the acoustic reactance. Also shown in Fig. 3.7 is an electrical matching network that consists of a series and a shunt inductor. The series resistor R_{se} is included in the realization that there will be a finite contact resistance to the top electrode and R_s is the source resistance of the signal generator. Typically R_{se} will be a few tenths of an ohm and R_s will be 50 ohms.

For the transducers considered for use with the acoustic microscope, the acoustic radiation resistance will be 0.5 to 5 ohms while the reactive part of the input impedance ($X_a - 1/\omega C_o$) will be on the order of 50 ohms capacitive. The two inductors act to transform the impedance seen by the source such that it matches the electrical impedance of the source at the desired frequency of operation. This is important since the untuned two-way insertion loss will typically be 30 dB while the tuned insertion loss can be as low as 6 dB.

The two-way insertion loss of the transducer is measured by using the pulse echo technique. From the model of Fig. 3.7, ignoring the matching network, the untuned two-way insertion loss in decibels can

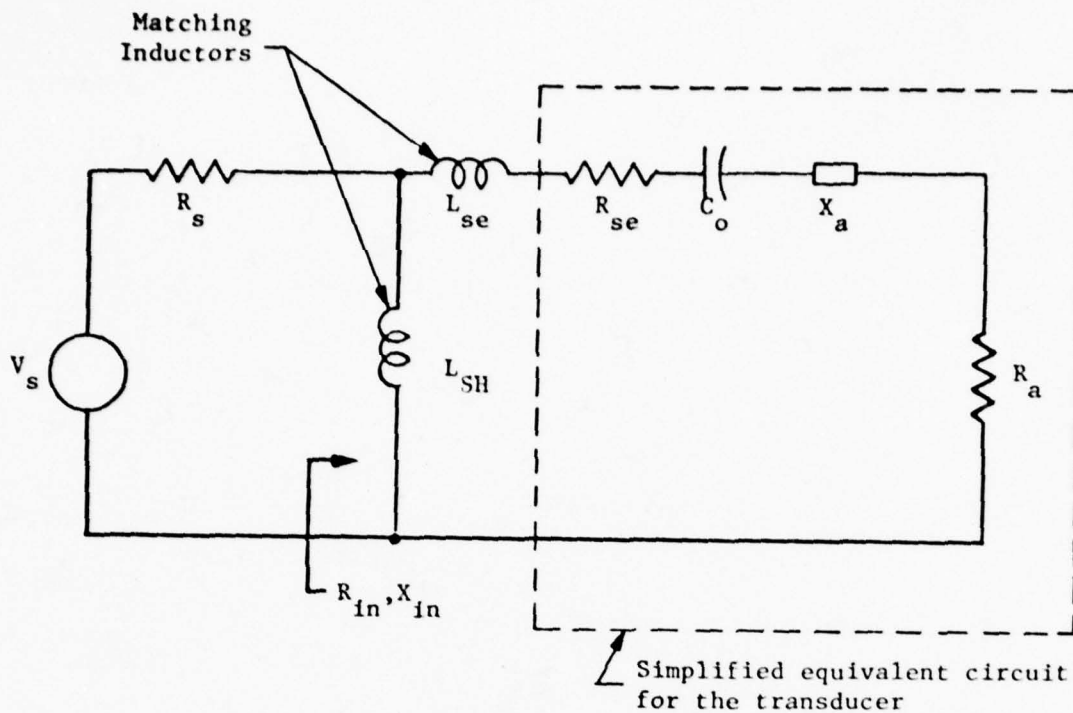


FIG. 3.7--Simplified equivalent circuit for the transducer with a two inductor matching network shown. With the matching network in place:

$$R_{in} = \frac{\omega^2 L_{SH}^2 (R_a + R_{se})}{(R_a + R_{se})^2 + X^2}$$

and

$$X_{in} = \frac{\omega L_{SH} (R_a + R_{se})^2 + X [\omega^2 L_{se} L_{SH} + \omega L_{SH} (X_a - (1/\omega C_o))]}{(R_a + R_{se})^2 + X^2}$$

where ω is the radian frequency and

$$X = \omega L_{se} + \omega L_{SH} + X_a - (1/\omega C_o) .$$

By adjusting L_{SH} and L_{se} it is possible to make $R_{in} = R_s$ with $X_{in} = 0$. Under these conditions the maximum amount of power is transferred to the load.

be easily shown to be;

$$\begin{aligned} \text{UIL} &= 20 \log \left(\frac{\text{Power Available}}{\text{Power to the Load } (R_a)} \right) \\ &= 20 \log \left\{ \frac{(R_s + R_{se} + R_a)^2 + [X_a - (1/\omega C_o)]^2}{4R_s R_a} \right\} \end{aligned} \quad (3.13)$$

while the two-way tuned insertion loss (i.e., the input to the transducer is matched to the source impedance) is given by;

$$\text{TIL} = 20 \log \frac{R_{se} + R_a}{R_a} \quad (3.14)$$

The above losses contain only the effects of the electrical properties of the transducer. Due to the measurement technique and the physical properties of the transducer there will be other expected losses. These include diffraction losses, attenuation losses and losses due to the top surface not truly being free over the entire area of the transducer.

The effects of acoustic diffraction on the measured properties of the transducer can be calculated by employing the results of Section B of this chapter. If a substrate material of length ℓ is used to measure the response of a transducer with the pulse echo technique, then the measured response will be reduced due to diffraction effects which take place over a length 2ℓ . In order to calculate the magnitude of this effect, the field at a distance 2ℓ from the transducer can first be calculated using Eq. (3.3) and then this field can be integrated over the transducer area to give the output voltage of the

transducer, i.e.,

$$V_{out} \propto \int_0^{2\pi} \int_0^{R_t} P(2\ell, r) r dr d\theta \quad (3.15)$$

This can be compared to the result that would be obtained without diffraction in order to see how diffraction affected the measured response. By calculating V_{out} as a function of ℓ it is possible to plot diffraction losses for a circular transducer as a function of the crystal length. In Fig. 3.8 the results of this calculation for a typical transducer are shown for both the isotropic and anisotropic sapphire case. The isotropic case is in good agreement with the results of Seiki.^{3.11} It can be seen that the diffraction effects for the isotropic case are stronger than they are for sapphire. This is expected since the anisotropy of sapphire tends to minimize the effects of diffraction by directing energy flow parallel to the c-axis. The losses due to diffraction should be added to the electrical losses predicted by Eqs. (3.13) and (3.14) before a comparison between experimental and theoretical results is made.

Additional loss will be observed in the measurement due to acoustic attenuation within the various materials. As part of the analysis the thin films that comprise the transducer were considered lossless, but clearly any acoustic attenuation within these layers will result in additional insertion loss. Also, attenuation in the sapphire rod will result in reduced measured efficiency, but this effect can be easily predicted. Longitudinal acoustic waves in

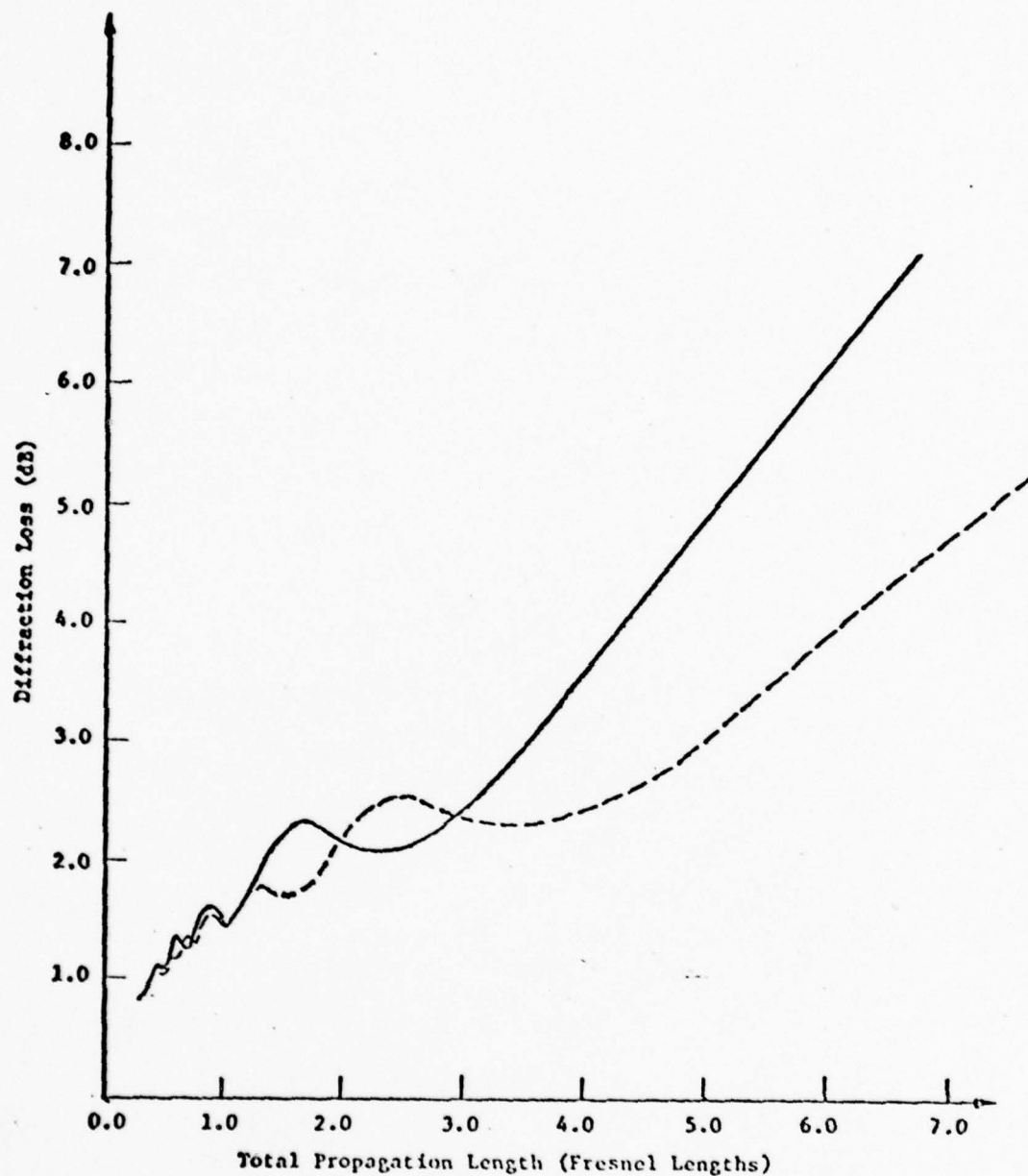


FIG. 3.8--Diffraction loss correction curves for piezoelectric transducers measured using the pulse echo technique. Solid line is for the isotropic case while the dashed curve is for sapphire.

sapphire are attenuated 0.3 dB/cm at 1 GHz and the loss will increase with the square of the frequency.^{3.12} Thus at a frequency of 3.0 GHz with a crystal length of 0.2 cm there will be an additional 1 dB measured insertion loss due to acoustic absorption in the sapphire.

A final loss mechanism within the transducer structure is concerned with the electrical bond made to the top surface of the transducer. This bond disturbs the assumed free surface for this electrode over the area of the bond and provides a path through which acoustic power can "leak out" of the transducer structure. If the area of the transducer is much greater than the area of the bond, then this effect will be negligible. This is true for most cases considered here. The effect of this bond could be calculated by considering the transducer structure to consist of two devices in parallel; one has an area equal to the transducer area minus the bond area and can be considered to have a free surface, and the second has a size equal to the bond area and a surface with an acoustic load of r_b , where r_b is the normalized mechanical impedance of the bond material. The analysis of the second transducer would be the same as the first except now Eq. (3.9) would become;

$$z_1 = - \frac{V_1/I_1}{R_o} = r_1 \frac{r_b \cos \theta_1 + j r_1 \sin \theta_1}{r_1 \cos \theta_1 + j r_b \sin \theta_1} . \quad (3.16)$$

In order to calculate the additional insertion loss of the device due to the bond, one would have to first calculate the insertion loss of

the parallel structure and then determine how much of the power is going into the bonding wire rather than into the substrate material. Even for the smallest transducers considered here, the bond area should never exceed 25% of the transducer area and thus the additional loss in the transducer due to this bond should not exceed 1-2 dB.

Based on the preceding analysis of the transducer a computer program was written to calculate both the tuned and untuned insertion loss for transducers used in the acoustic microscope. The effects of acoustic diffraction and attenuation are included within this calculation. A listing and brief description of this program is given in Appendix D.

In Fig. 3.9 a comparison between a theoretical and experimental transducer design is shown for both the tuned and untuned response. The ZnO was assumed to have a k_t of 0.20 (as compared to the bulk value of 0.28) and the series loss resistance R_{se} was 0.5 Ω . The experimental measurements were made using the pulse echo technique. The untuned insertion loss measurements agree well with theory, and therefore, the choice of $k_t = 0.20$ seems to be valid. The measured tuned insertion loss agrees well in form to the calculated values, but the bandwidth is somewhat reduced and typically the measured result is 2-3 dB greater than the calculated one. The minimum two-way insertion loss was 5.5 dB for this device at 1.0 GHz.

Results for a similar device designed to work in the 1.8-2.8 GHz frequency range are shown in Fig. 3.10. The minimum two-way tuned insertion loss for this device was 11.0 dB at 2.0 GHz. For the theoretical calculation k_t was taken as 0.20 and R_{se} as 1.0 ohm. Reasonable agreement between theory and experiment was obtained for

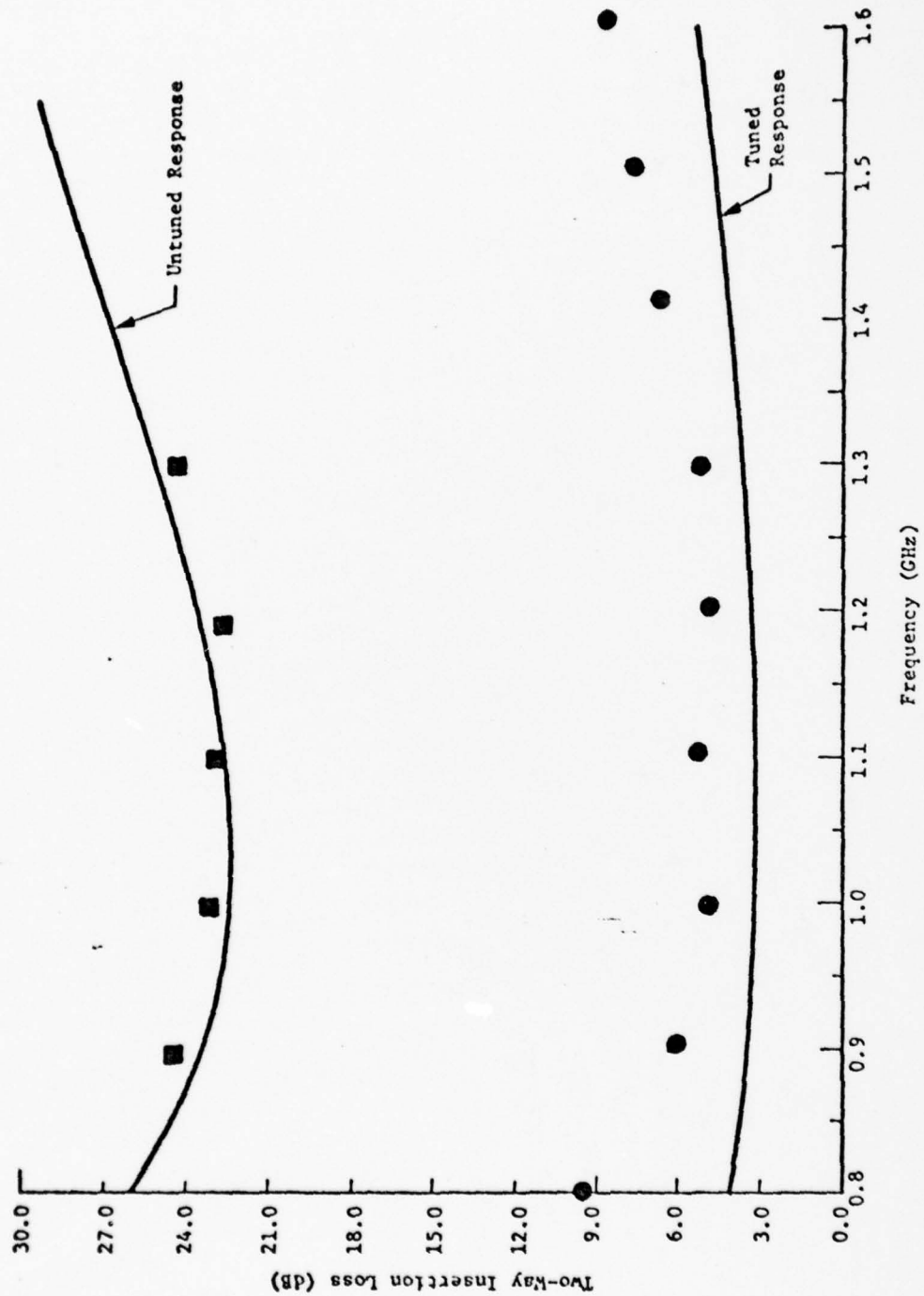


FIG. 3.9--Comparison of theoretical and experimental response for a Au-ZnO-Au-Al₂O₃ transducer. Squares are measured untuned values and circles are measured tuned values. Transducer geometry is $R_t = 100 \mu\text{m}$, $t_o = 1.6 \mu\text{m}$, $t_1 = t_2 = 0.2 \mu\text{m}$, $l = 2000 \mu\text{m}$, $k_t = 0.20$ and $R_{se} = 0.5 \text{ ohms}$.

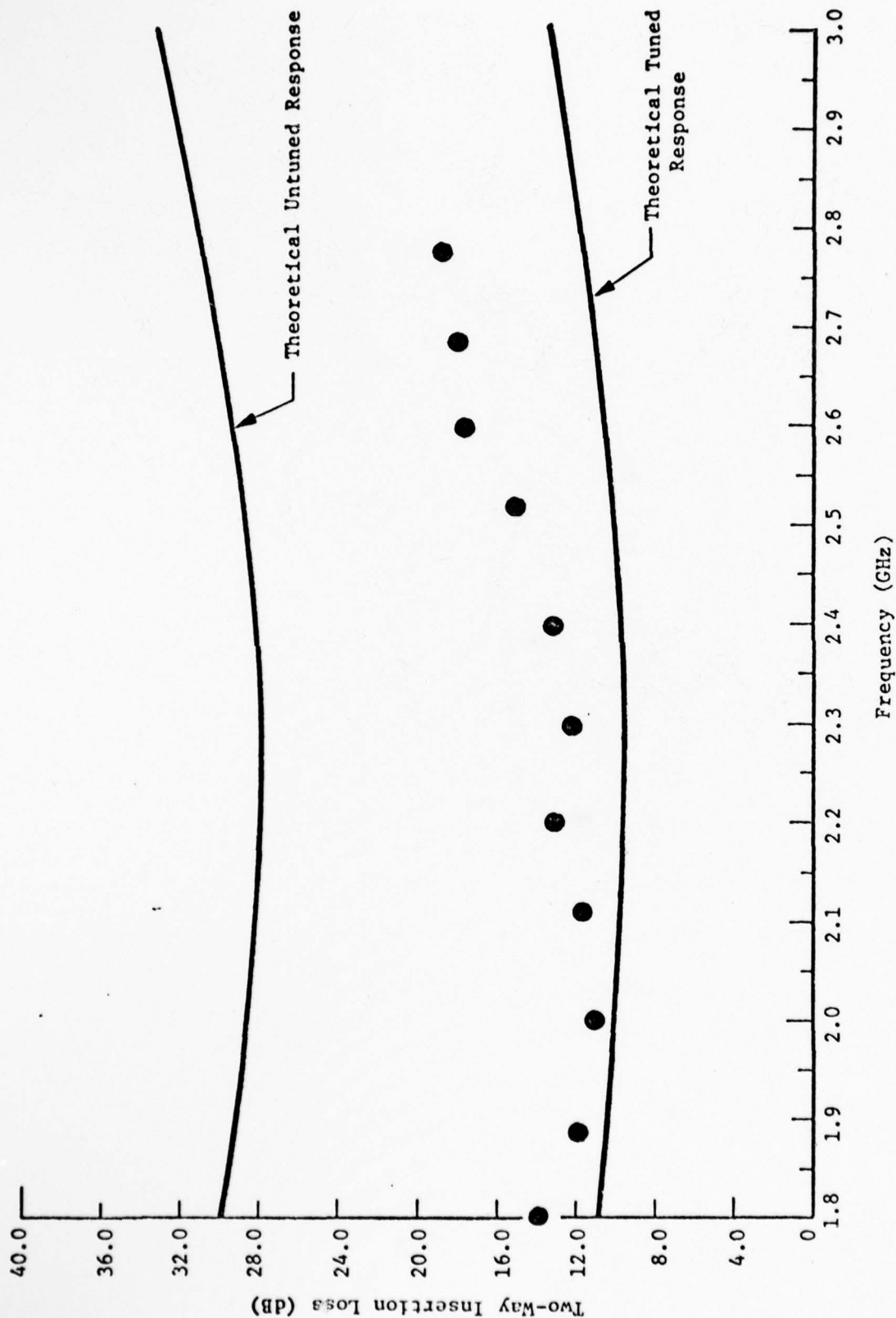


FIG. 3.10--Comparison between theoretical and experimental response for a Au-ZnO-Au-Al₂O₃ transducer. The circles are measured tuned results. The geometry of the transducer is $R_t = 125 \mu\text{m}$, $k_t = 0.20$, $t_o = 0.6 \mu\text{m}$, $t_1 = t_2 = 0.1 \mu\text{m}$, $\lambda = 2000 \mu\text{m}$ and $R_{se} = 1.0 \text{ ohm}$.

frequencies between 1.8 and 2.4 GHz, but at the higher frequencies the measured loss was significantly higher than predicted (as much as 7 dB). This indicates that the bandwidth of the device is somewhat restricted, but it also reflects the fact that it is more difficult to tune these devices at the higher frequencies.

The tuned insertion loss measurements described above were all made by tuning each point individually using double stub tuners. The bandwidth of these devices is typically 10 MHz, and therefore, not adequate for matching the short pulses that are used in the microscope. For this reason the matching network shown in Fig. 3.7 is used to match the transducers used with lenses. The tuned theoretical response for a transducer designed to operate at 2.8 GHz is shown in Fig. 3.11. Also shown are two theoretical response curves for two matching network configurations. The first curve is for $L_{se} = 0.1 \text{ nH}$ and $L_{SH} = 0.55 \text{ nH}$. This matching network results in a nearly perfect match over a bandwidth of 300 MHz, however, it is difficult to implement due to the extremely small series inductance required. A more realistic design is shown in the second curve where L_{se} is 0.25 nH and L_{SH} is 0.4 nH. Inductors this small are difficult to realize, but it is possible to do so by using the self-inductance of the gold wires that are bonded to the top dot and the counter electrode. For a 2 mil gold wire the self-inductance is approximately 1 nH/mm and thus lengths less than 1 mm are necessary. In order to tune the lenses at frequencies above 2.0 GHz using this technique it is necessary to do all work under a microscope. A 50-ohm micro-strip

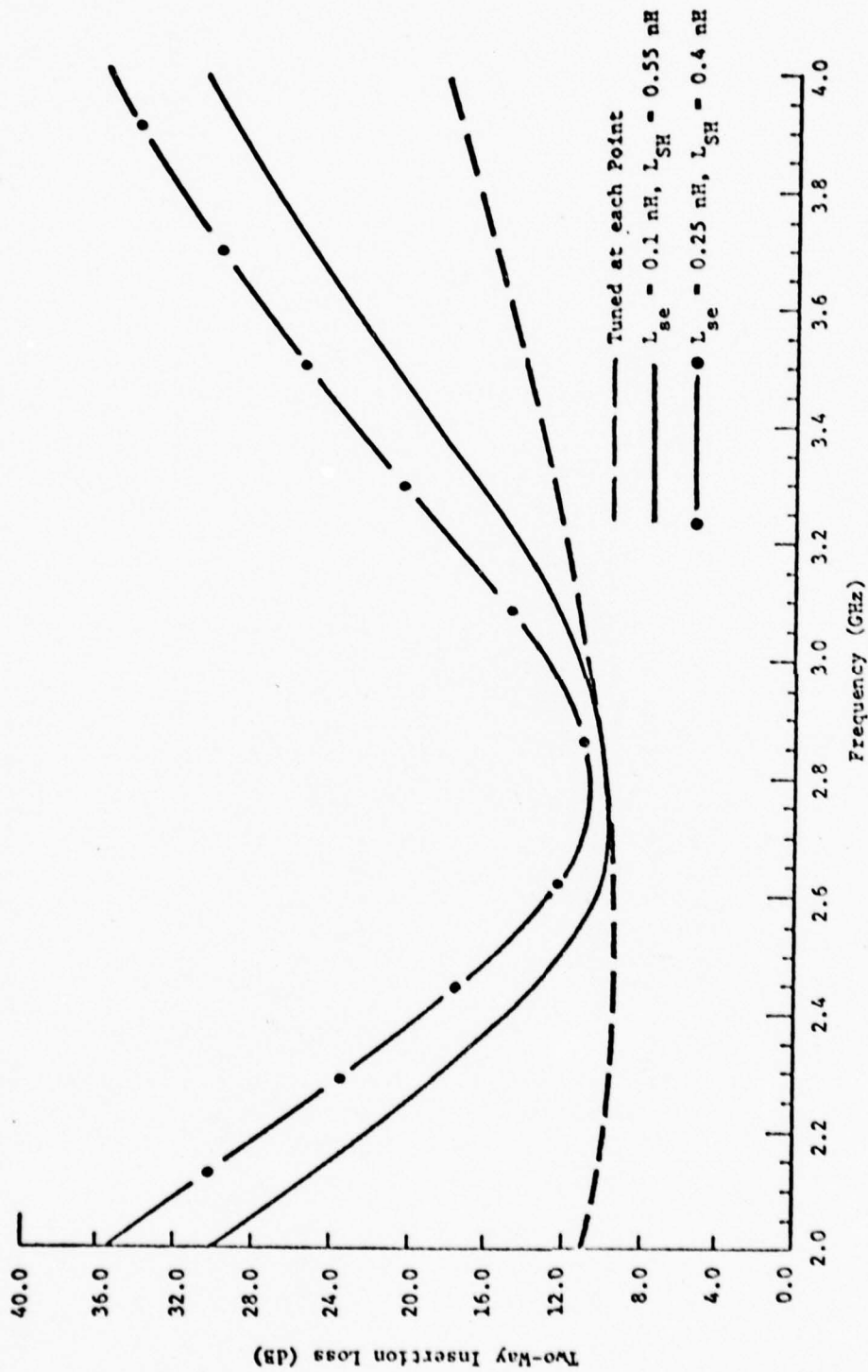


FIG. 3.11--Theoretical response of an Au-ZnO-Au-Al₂O₃ transducer under various matching conditions. Geometry of transducer is $r_1 = 100 \text{ } \mu\text{m}$, $r_0 = 0.5 \text{ } \mu\text{m}$, $t_1 = t_2 = 0.1 \text{ } \mu\text{m}$, $l = 2000 \text{ } \mu\text{m}$, $k_t = 0.20$ and $R_{se} = 1.0 \text{ ohm}$.

transmission line is run to within 0.25 mm of the top electrode and the series and shunt inductors are connected using silver epoxy. The inductors are varied using a toothpick until the input pulse to the device is well matched. The device is considered to be well matched if the power level of the input pulse is reduced by 10 dB or more. The resulting bandwidth can be checked to see if it is adequate to pass the short pulses used in the microscope by examining the first echo from the lens surface. If it is not spread in time duration as compared to the input, then the bandwidth is sufficient. A more thorough examination can be performed if a network analyzer is available in the appropriate frequency range. Bandwidth is usually not a problem with these matching networks since only 5 - 10% 3 dB bandwidth is required.

In conclusion, transducers with two-way insertion loss of 6 dB can be designed and fabricated at frequencies around 1 GHz. At frequencies above 2.0 GHz the two-way insertion loss increases to approximately 11 dB, and the fabrication of matching networks becomes more difficult due to the small size of the inductances required. At frequencies above 4.0 GHz it will be extremely difficult to form electrical matching networks using the techniques described here.

E. Acoustic Matching Layers

At the lens liquid interface there is an acoustic impedance mismatch which can result in a large acoustic reflection coefficient, and consequently poor power transfer across the boundary. Since this will reduce the dynamic range of the microscope it is desirable to minimize the reflection coefficient. This can be accomplished by using a material of intermediate acoustic impedance to act as an acoustic transformer between the lens and the liquid. The analysis of this transformer is difficult for the geometry of the acoustic lens since the problem must be solved as a function of the incidence angle and the integrated effect over the entire lens must be considered. In this section the design, fabrication and evaluation of acoustic matching layers are considered. In particular a single layer of borosilicate glass (9741 from Corning Glass Works) sputtered directly on the lens surface is found to yield an excellent matching layer. This film exhibits good adhesion to the sapphire lens and excellent mechanical stability. The properties of this glass are evaluated and its predicted matching efficiency is compared with experimental results for the normal incidence case. The transfer function of the acoustic lens is calculated in the presence of this matching layer for various glass profiles. It is found that the matching layer reduces the two-way insertion loss across the boundary by up to 15 dB and its thickness profile can be used to modify the spatial frequency response of the lens.

The motivation for using an acoustic matching layer can be readily appreciated by considering the simple geometry of Fig. 3.12A.

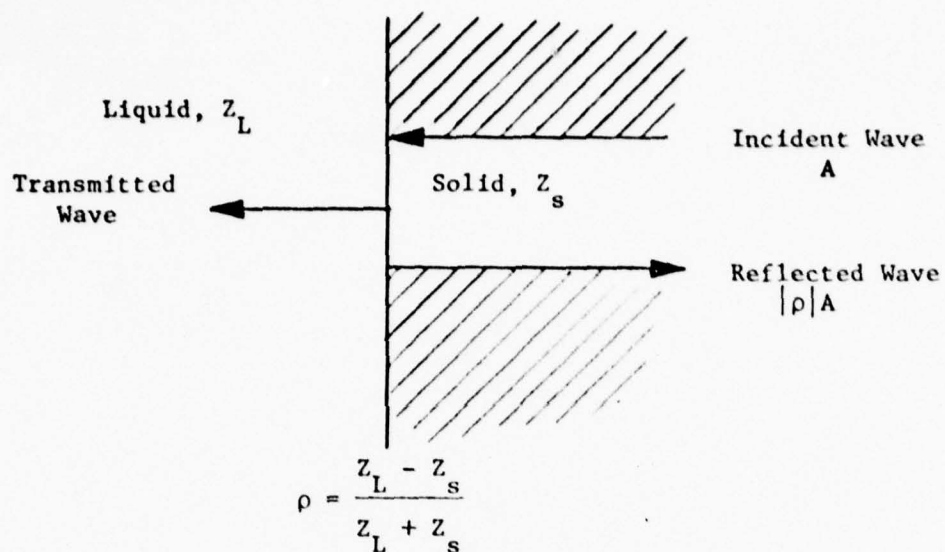


FIG. 3.12--(a) Reflection of acoustic waves at a solid-liquid boundary.

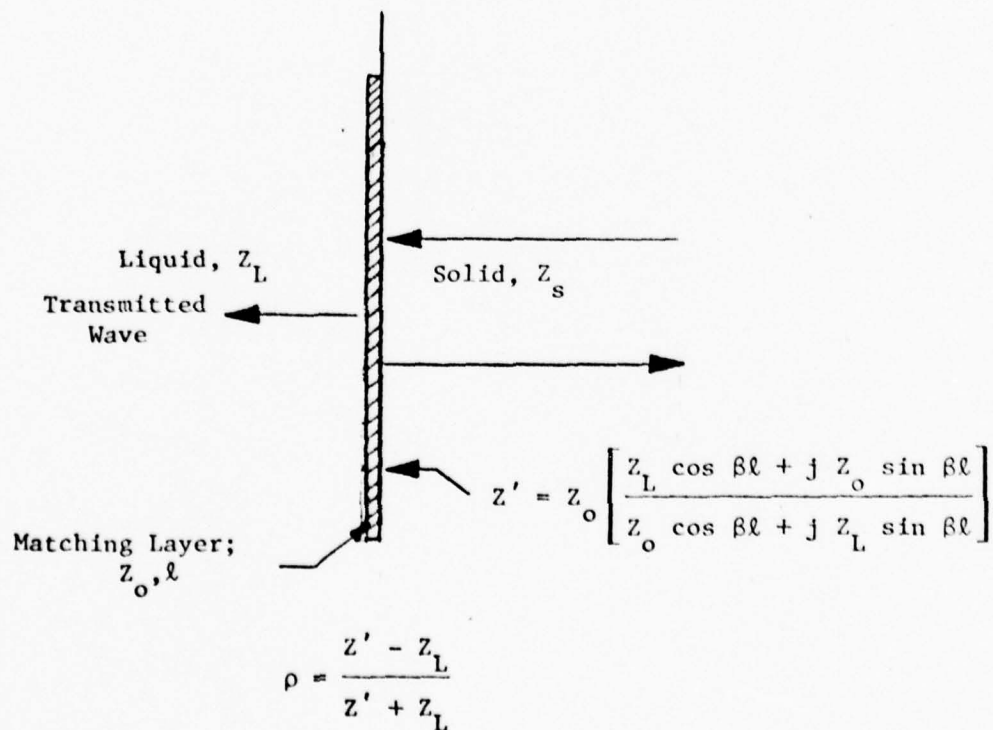


FIG. 3.12--(b) Reflection of acoustic waves at a solid-liquid boundary with an antireflection coating.

Here a longitudinal acoustic wave is normally incident onto a solid-liquid interface. The mechanical impedance of the solid is z_s g/cm²-sec while the liquid is z_l g/cm²-sec. If the incident wave has amplitude A then the reflected wave in the solid will have an amplitude $|\rho|A$ where^{3.13}

$$|\rho| = \left| \frac{z_l - z_s}{z_l + z_s} \right| . \quad (3.17)$$

For a sapphire-water interface $z_s = 44.0 \times 10^5$ g/cm²-sec and $z_l = 1.5 \times 10^5$ g/cm²-sec, and thus $|\rho| = 0.934$. This means that 87% of the incident power will be reflected. For the acoustic lens this boundary must be crossed twice which implies only 1.6% of the incident power would return even if no other loss mechanisms were present. This results in a two-way insertion loss across the boundary of 17.9 dB.

Now consider the geometry of Fig. 3.12B where an intermediate layer of material with mechanical impedance z_o is included between the liquid and the solid. Using the results from lossless transmission line theory (this is acceptable since the electromagnetic case is a direct analog to the case considered here), the impedance seen at the solid-matching layer interface looking toward the liquid is given by;^{3.13}

$$z' = z_o \left[\frac{z_l \cos \beta l + j z_o \sin \beta l}{z_o \cos \beta l + j z_l \sin \beta l} \right] \quad (3.18)$$

where $\beta = 2\pi/\lambda$, λ is the acoustic wavelength in the matching layer and ℓ is the matching layer thickness. The reflection coefficient at the boundary will now be

$$|\rho| = \left| \frac{z' - z_s}{z' + z_s} \right|. \quad (3.19)$$

If $z' = z_s$ then all the power can be transmitted into the liquid. This can only happen if z' is real and not equal to z_ℓ , and therefore, can occur only if $\ell = n\lambda/4$ and $z_o = \sqrt{z_\ell z_s}$ where n is an odd integer. Thus in order to effectively match the acoustic energy across the boundary, a material whose mechanical impedance is the geometric mean of the mechanical impedance of the solid and the liquid is needed. This material must be compatible with thin film growth techniques since from bandwidth considerations the matching layer should be $\lambda/4$ thick. It must also be mechanically hard so as not to be subject to scratching. For a sapphire-water interface a material with an acoustic impedance of 8.12×10^5 gm/cm²-sec is required. Unfortunately it is not possible to find a material that meets all of the above criterion simultaneously. In fact it is difficult to even find a material with the desired mechanical impedance. Figure 3.13 summarizes the velocity, density and mechanical impedance of several materials.^{3.14} It can be seen that the region around a mechanical impedance of 8.0×10^5 gm/cm²-sec is empty. There is some evidence that carbon^{3.15} and glass^{3.16} films can be sputtered in such a manner that the mechanical impedance of the film will present

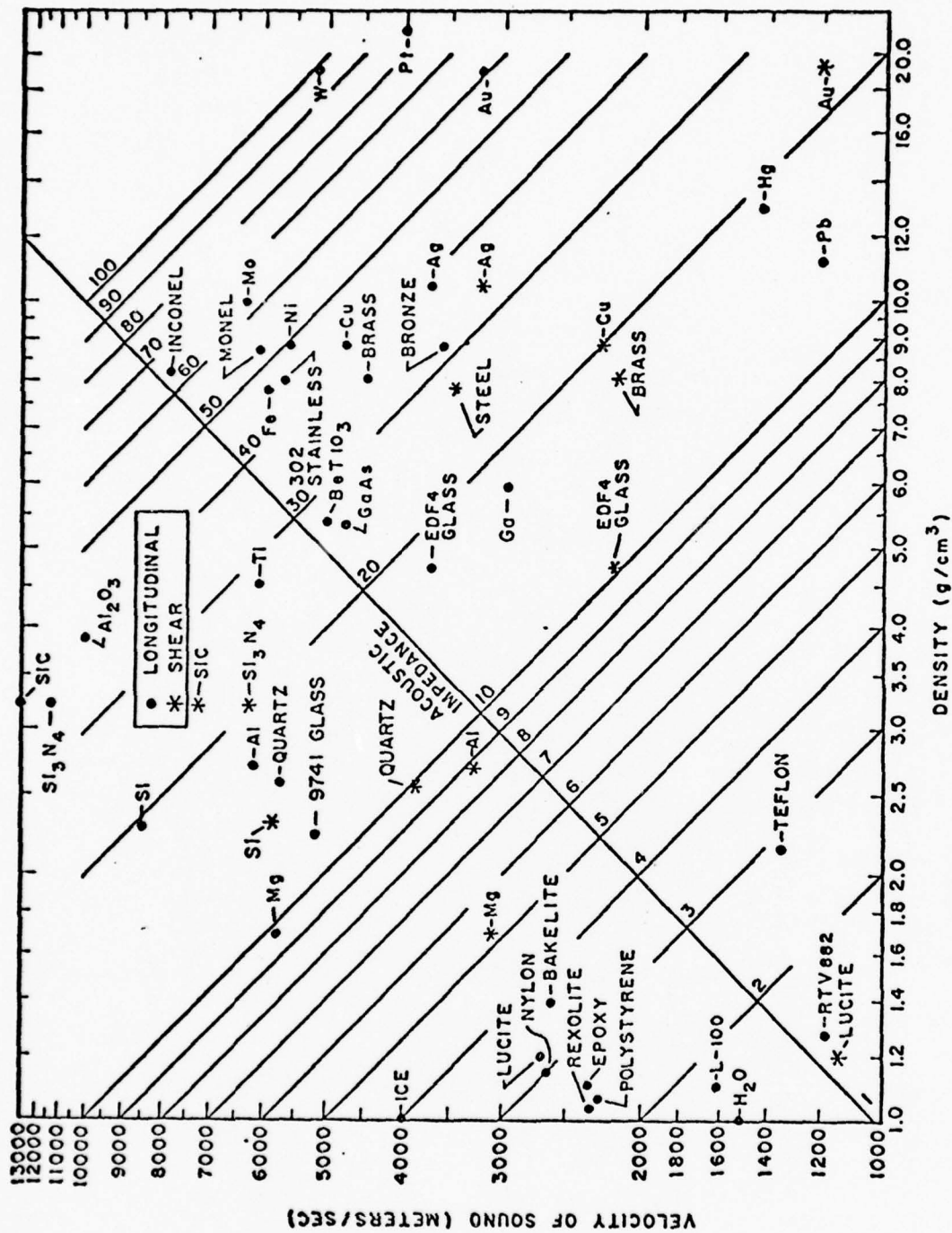


FIG. 3.13--Acoustic properties of materials (after Eggleton^{3.14}).

a better mechanical matching layer than their bulk values would indicate.

It is possible to use multiple matching layers to compensate for the fact that no single material ideally suits the requirements of a sapphire-water boundary. These layers must adhere well to the sapphire and to each other and must meet the same mechanical toughness standards that are imposed on a single layer. A good candidate structure for a two-level matching network is a $\lambda/4$ coating of gold ($z = 61.3 \times 10^5 \text{ g/cm}^2\text{-sec}$) followed by a $\lambda/4$ coating of glass ($z = 11.6 \times 10^5 \text{ g/cm}^2\text{-sec}$). By repeated application of Eq. (3.18) and use of Eq. (3.19) it is found for this case that $|\rho| = 0.028$. This results in 99.9% of the energy being transferred across the boundary, i.e., almost a perfect match. These layers have adhesion problems, but with the appropriate interface layers they would make excellent matching layers. Of course, the above calculations are for a flat surface and the matching properties for a lens will not be as good. The price for multiple matching layer geometries is smaller bandwidth and added fabrication difficulty. It is also necessary to accurately control the thickness of the two layers.

Very little is gained (approximately 1 dB) by using a double matching layer as opposed to a single layer when considering the power transfer through the acoustic lens. The motivation for going to a double layered structure is to greatly reduce the amount of power reflected from the lens liquid interface. It would greatly simplify the pulse electronics of the microscope if this reflection could be reduced by 30 - 40 dB below its current value. This nearly

ideal match could be obtained by using either a multilayered acoustic transformer, or by attempting to control the fabrication parameters of a single layered transformer such that the appropriate mechanical impedance is obtained. The acoustic impedance of a material is given by the product of its acoustic velocity and its density. If a thin film is fabricated at a high rate onto a cold substrate it tends to have reduced density^{3.16} and thus lower acoustic impedance if its velocity is not greatly affected. In Fig. 3.14 is shown the calculated return loss from a flat surface with a $\lambda/4$ acoustic transformer whose mechanical impedance is allowed to continuously vary. It can be seen from this that if an additional 30 dB of return loss is desired, the effective impedance of the acoustic transformer (either a single or multilayered structure) would have to be between 8.05×10^5 and 8.20×10^5 g/cm²-sec. This is a narrow range, but it should be attainable with the appropriate fabrication of a gold-glass transformer.

Primarily as a fabrication convenience only single layered acoustic transformers are presently being used in the microscope. Borosilicate glass has been utilized in this work due as much to its mechanical stability and toughness as to its relatively close acoustic impedance match to the desired value. With a $\lambda/4$ coating of this glass the reflection coefficient drops from 0.934 to 0.342 for the normal incidence case. Under these conditions 88.4% of the energy will be transmitted across the boundary and the two-way insertion loss will be 1.1 dB; a reduction of 16.8 dB from the no-matching layer case.

The above calculations are based on the measured bulk properties of the glass and it is not assured that the thin film properties will be

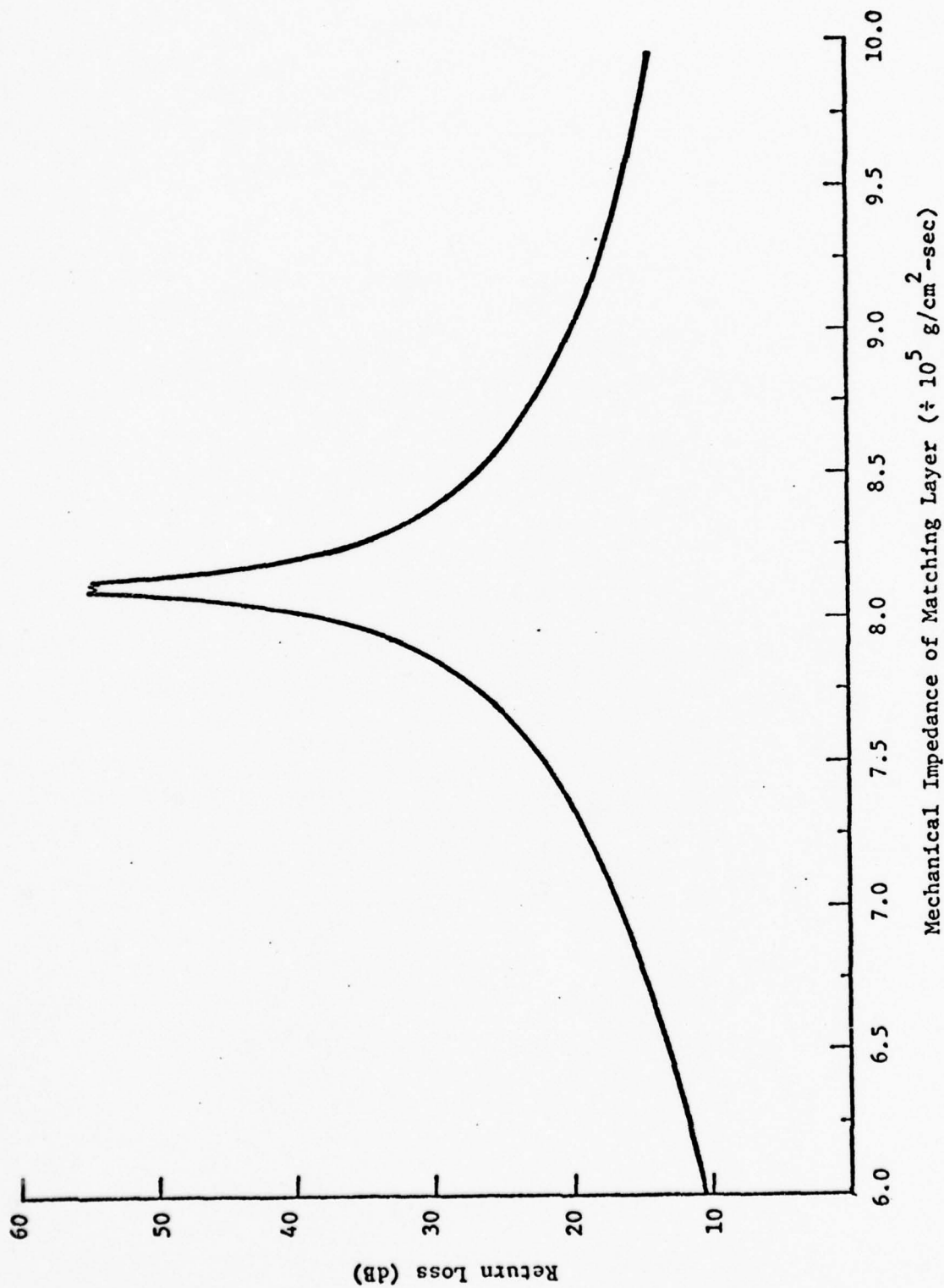


FIG. 3.14--Return loss as a function of the effective acoustic impedance of the transformer.

the same. In order to check the properties a piezoelectric transducer was fabricated on one end of a sapphire rod and a $\lambda/4$ coating of glass was deposited on the opposite end. The glass was deposited by RF sputtering from a circular glass target. Using a pulse echo technique, the magnitude of the first reflected pulse from the sapphire-glass interface was measured as a function of frequency for both the case where the glass layer was loaded with air and with water. For the air case $|\rho| \approx 1.0$ while for the water case at the $\lambda/4$ condition $|\rho| = 0.342$, and therefore, it is expected that the addition of the water under these conditions should result in the reflected signal being reduced by 9.3 dB. In Fig. 3.15 a plot of this return loss measurement as a function of frequency is shown along with the theoretically predicted value. It can be seen that the theoretical result is in agreement with experiment, and thus the bulk properties of the film seem to be a good approximation to the thin film properties.

All evaluation to this point has been based on a flat interface, but the matching layer must be used on the curved surface of the lens. Therefore, the efficiency of power transmission should be calculated as a function of angle of incidence with respect to the spherical lens surface and the integrated effect over the entire lens evaluated. This is a complicated problem, but it has been solved by Brekhovskikh^{3.17} for an arbitrary number of layers. A computer program based on this analysis was developed by Lemons^{3.18} and it has been used to calculate the transmission function of the acoustic lens under various conditions. Due to the fabrication technique used for the glass layer, its

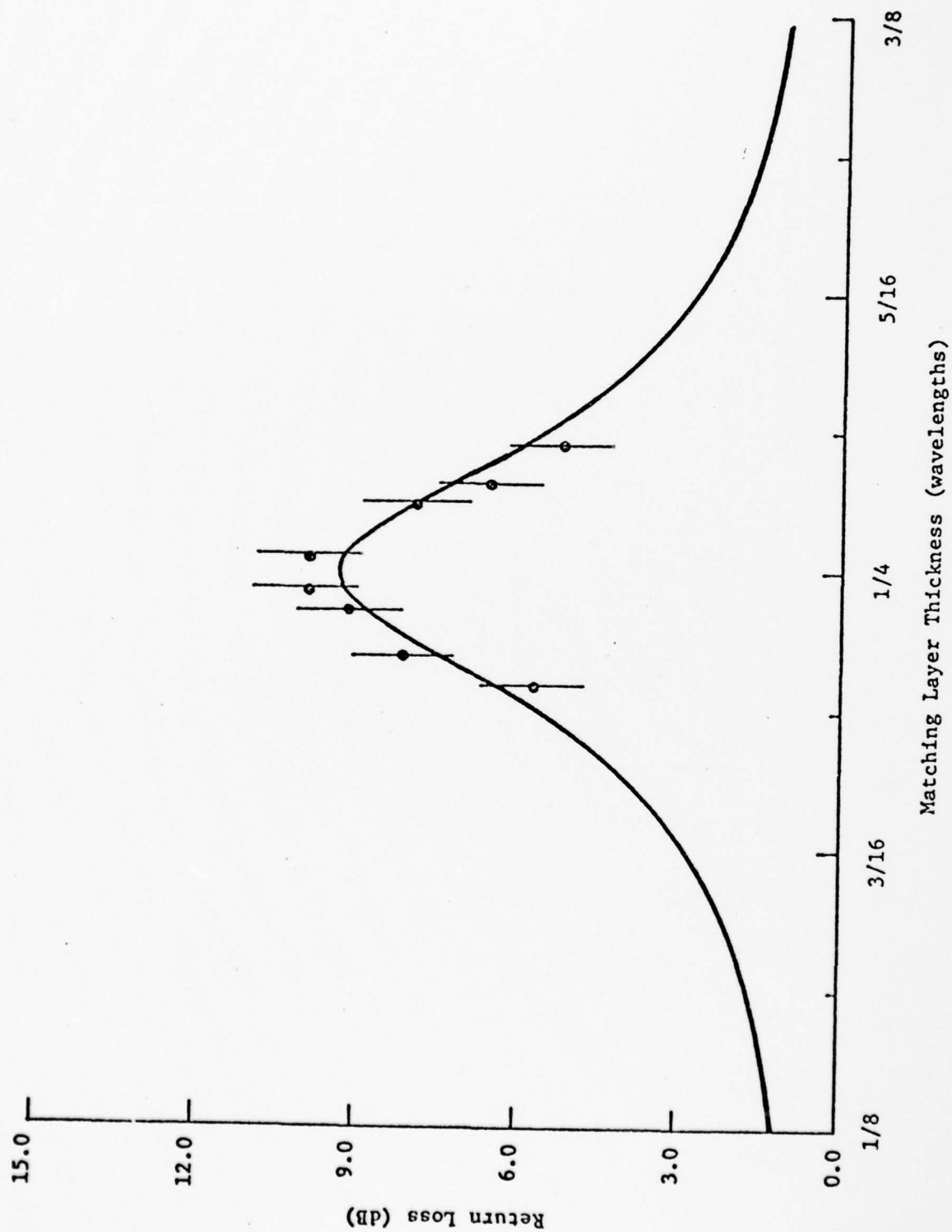


FIG. 3.15---Comparison between the theoretical response of a glass transformer based on its bulk properties and the experimental result.

thickness will vary approximately as the $\cos(\theta)$ where θ is the angle between the lens axis and the perpendicular to the plane of tangency of the lens surface. In Fig. 3.16 the transmission function of the acoustic lens is shown for 4 cases. Case #1 is with no matching layer at all. In case #2 the glass thickness is chosen such that it is $\lambda/4$ at the center of the lens while in case #4 the glass thickness is $\lambda/4$ thick at the outer edge of the lens. Finally, in case #3 a compromise between cases #2 and #4 is selected with the glass thickness chosen to be 0.31λ at the lens center with the result that it is 0.2λ at the outer edge of the lens (assuming a maximum opening angle for the lens of 50°).

In Fig. 3.17 the resulting lens focal plane distribution for each of these lens transmission functions is shown normalized to the same value. The focal plane response for case #1 is also repeated without normalization. It can be seen by comparing case #1 without normalization with case #2 that integrated over the lens surface the matching layer results in a two-way transmission improvement of 13.9 dB. The best matching layer from a power transmittance point of view is case #3 which results in a two-way insertion loss improvement of 15.2 dB. This is easily understood from the lens transfer function for this case which is shown in Fig. 3.16. Although this transmission is less than for case #1 at low angles, it is higher at the larger angles where most of the lens area is located. Case #4 results in only an 11.2 dB power transfer improvement over the no matching layer case, but in most instances it is the best choice from an imaging point of view. By

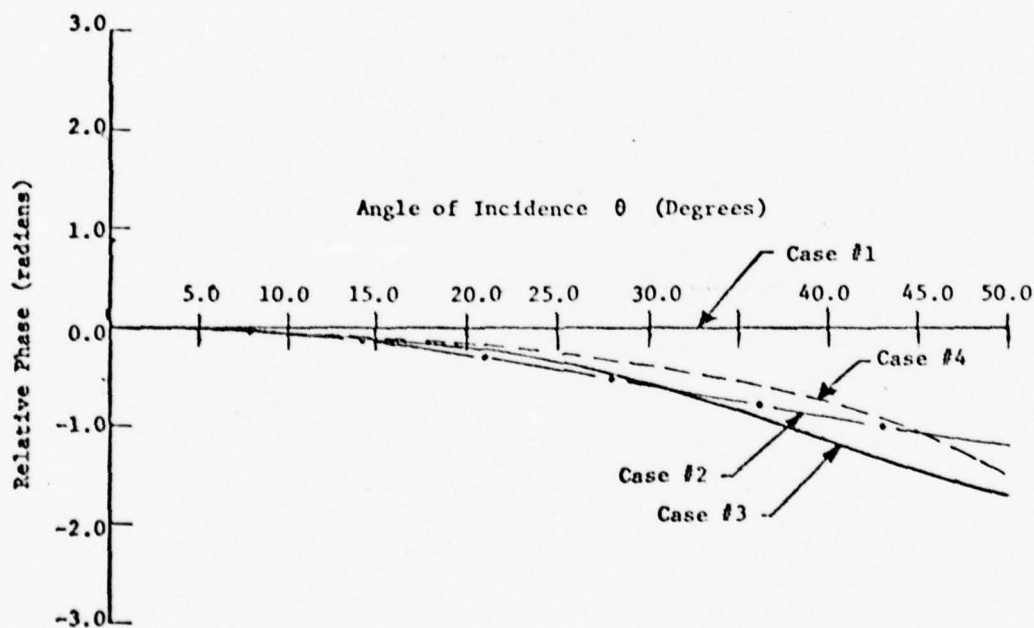
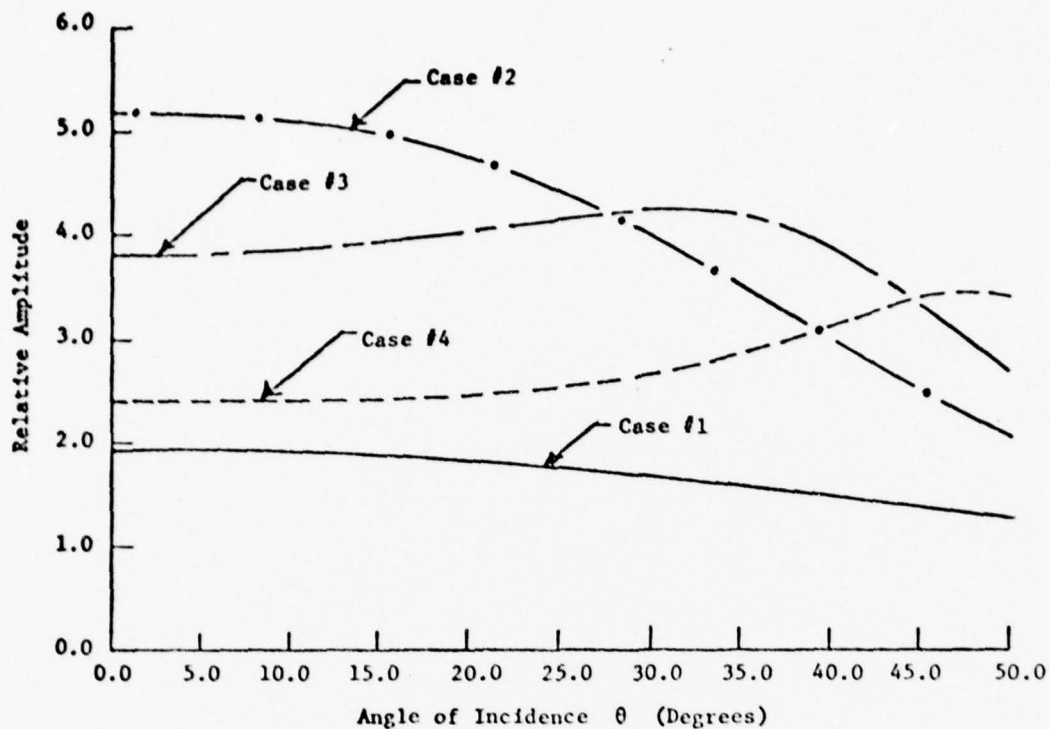


FIG. 3.16--Lens transmission function for various glass thicknesses assuming a $\cos(\theta)$ dependence. Case #1 - no glass; Case #2 - 0.25λ , Case #3 - 0.31λ and Case #4 - 0.39λ . Thicknesses refer to the center of the lens.

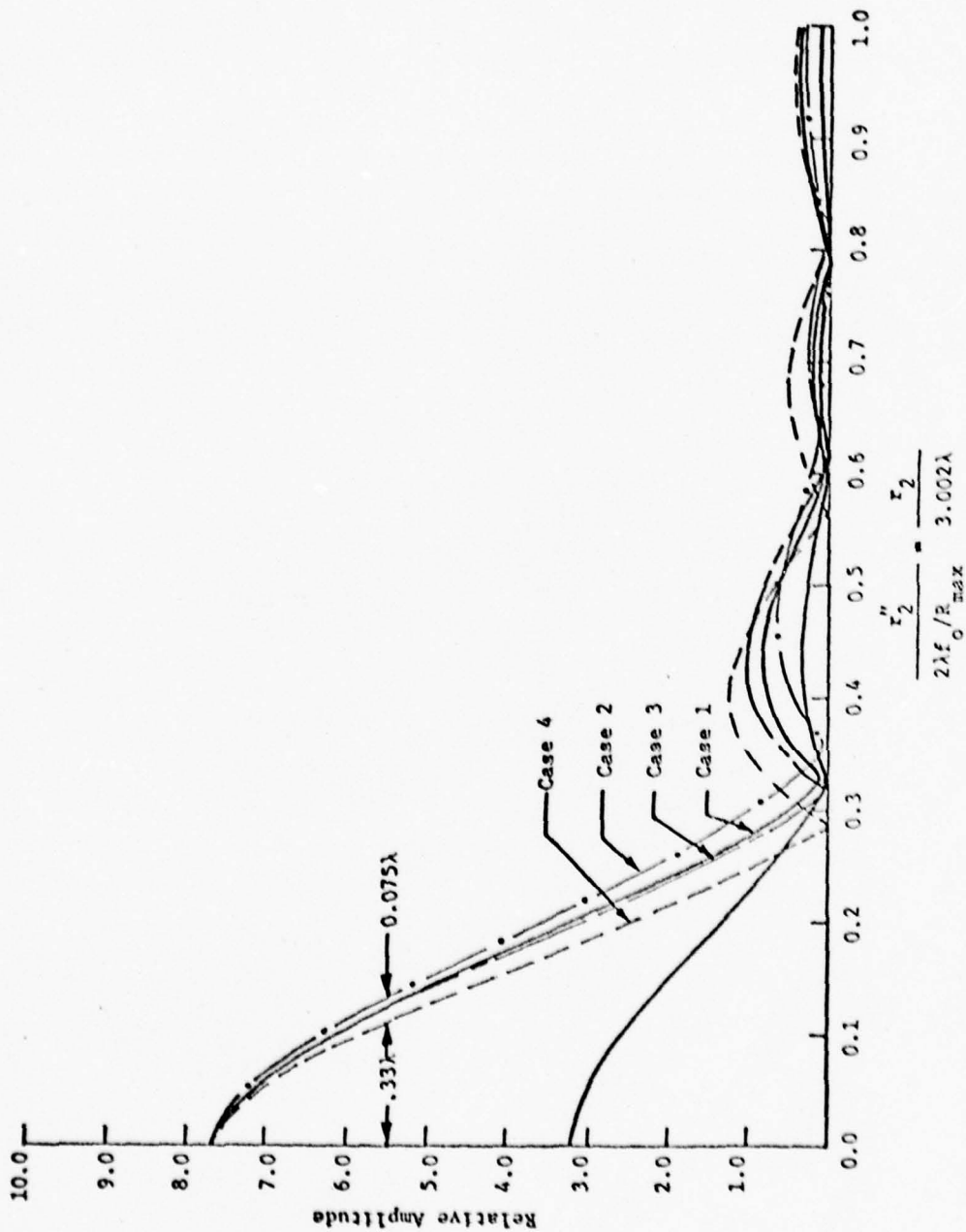


FIG. 3.17--Focal plane response of the acoustic lens as a function of the glass thickness assuming a $\cos(\theta)$ dependence. Case #1 - no glass; Case #2 - 0.25λ , Case #3 - 0.31λ and Case #4 - 0.39λ . Thicknesses refer to the center of the lens. All other parameters are held constant.

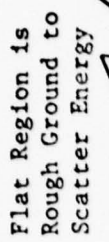
having the best acoustic match at the outer edge of the lens it is possible to compensate for the effects of diffraction which results in reduced power density in this region. As can be seen from Fig. 3.17, the 3 dB focal beam width is 0.8λ for case #2 while it is reduced to 0.65λ for case #4. This width is approximately 0.75λ for both the no glass case and the 0.31λ case. Thus it is possible to reduce the beam width by approximately 15% if an additional 4 dB of acoustic loss is accepted. Alternately, the acoustic frequency could be increased by 15% to accomplish the same thing but the additional acoustic absorption would be much greater than 4 dB. For instance, for a liquid whose acoustic absorption increases with frequency squared and assuming an initial liquid absorption of 60 dB, the additional loss to get a 15% resolution improvement would be 19.4 dB. The additional price one pays for using the lens transmission function of case #4 is an increase in side-lobe levels as shown in Fig. 3.17. However, these side-lobes are still down by 16 dB from the main lobe and should present no difficulty.

F. Lens Design

This section has been concerned with the various phenomena that affect the design and operation of the acoustic lens. In this section two typical lens designs are presented in an effort to bring these concepts together. In designing the acoustic lens it is desirable for its focal width to be as small a fraction of an acoustic wavelength as possible without incurring unreasonable acoustic losses due to diffraction effects. Ignoring for the moment the factors that affect the generalized pupil function of the acoustic lens as described in Chapter II,

the focal width of the acoustic lens will be proportional to the F-number of the lens. This number is given by the focal length of the lens divided by its aperture diameter (i.e., $F\text{-number} = F_o / 2r_l \sin \theta_{\max}$ where F_o is the focal length, r_l is the lens radius and θ_{\max} is the maximum opening angle of the lens). Due to spherical aberration effects and the desire to maintain working space between the lens and the object to be studied, the maximum opening angle for a sapphire-water lens is usually limited to 50 degrees. Thus the F-number for the lens is set at 0.75. In Fig. 3.18 is a diagram of a typical acoustic lens. The lens radius usually determines the maximum frequency at which the microscope can be operated while the transducer radius r_t and the crystal length d will be determined by diffraction effects. The parameters of the piezoelectric transducer (t_o, t_1, t_2) will be determined by the frequency of operation as will the glass thickness t_g which can be chosen to correct somewhat for the effects of diffraction.

When designing an acoustic lens to operate in water one would normally start with some resolution performance in mind. With an F.75 lens, 0.7λ resolution is reasonable to expect and thus the resolution requirement will set the acoustic wavelength which in turn determines the frequency of operation. In order to specify what radius acoustic lens will be needed it is necessary to know what total acoustic loss can be tolerated in the water path and the temperature at which the microscope will be operated. The total loss acceptable in the liquid path will be determined primarily by the electronic detection scheme utilized, but it will also be



50, $t_1 = 0.1 \mu\text{m}$, $t_2 = 0.3 \mu\text{m}$, $t_3 = 0.72 \mu\text{m}$, $d = 2 \mu\text{m}$, $D = 1 \mu\text{m}$. The two bonding wires shown connected to the counter-electrode would only be necessary for the higher frequency

affected by losses within the lens element and signal-to-noise requirements for the image. The temperature at which the water can be utilized will be dependent upon the samples examined. It is advantageous to heat the water as much as possible if the samples are compatible with the elevated temperatures. If the total loss (T.L.) is specified in decibels and the maximum temperature of the water is given such that the minimum Figure of Merit (FM) is known, then the maximum lens radius is approximately given as;

$$r_{\ell} = \frac{T.L. \times (FM)^2}{0.460 \times f^2} \mu m \quad (3.20)$$

where f is the necessary frequency of operation normalized by 1.0 GHz.

Unfortunately lens design is usually dictated by the availability of the acoustic lens and thus r_{ℓ} is known a priori. The maximum frequency of operation f is selected using Eq. (3.20) such that the total liquid losses will not exceed the desired limit under the imposed operating conditions. Once the frequency is known it is possible to specify the crystal length d and the transducer radius r_t by examining the lens illumination under various circumstances. The crystal length is typically chosen as 1-4 Fresnel lengths (r_t^2/λ) and r_t is generally 1-2 times as large as the radius of the lens aperture. These dimensions are more precisely defined by calculating the beam profile for a few cases using the diffraction program of Appendix C. Typically the design is such that the outer extremities of the lens receive 3 dB less power density than the central regions. The design of the transducer does not usually require a computer solution although

the computer program of Appendix D can be quite useful in finding the necessary values for the inductances used to electrically match the transducer. The thickness of the ZnO is approximately given by;

$$t_o = 1.6/f \text{ } \mu\text{m}$$

where f is the center frequency of operation normalized by 1 GHz. The gold contact electrodes are selected to be electrically thin with $0.1 \text{ } \mu\text{m}$ usually taken as a lower limit. Finally, as described in Section E, the glass thickness can be selected based on the frequency of operation and it is generally between 0.3 and 0.39 acoustic wavelengths thick at the lens center.

Referring to Fig. 3.18 it can be seen that the front end of the lens element is beveled to a point that is approximately twice as large as the lens aperture. This keeps the body of the lens element away from the object under study and makes it easier for the operator to see how close the lens is to the object. The flat region around the spherical cavity that constitutes the lens itself is usually rough ground in order to act as a scatterer of any acoustic energy that falls outside the aperture of the acoustic lens. This minimizes the amount of energy that passes through the flat region, reflects from the object and returns to coherently interfere with the information return.

The diameter of the lens element (D) is usually 0.25 inches. This value is selected as a matter of handling convenience and

smaller values are certainly acceptable. The gold wires shown connected directly to the counter-electrode are used only on the high frequency lenses (2 GHz and above) and are necessary due to the small value of the tuning inductors essential at the higher frequencies.

Lemons^{3.18} previously described the fabrication of the spherical cavity that constitutes the lens. The process becomes more difficult for the smaller radius lenses, primarily due to the difficulty in forming an initial starting hole from which the lens can be polished. This is presently accomplished by first coating the lens with a thin film (either metal or plastic) and then forming a small hole in this relatively soft film to act as a guide for the tool that forms the starting hole. Once a hole of appropriate size is formed the lens is polished using a tungsten tip and diamond polishing compounds in the same manner as described by Lemons.

Based on the preceding considerations two lens designs will be considered. First a 100 μm radius lens that can be utilized at room temperature with a maximum water loss of 60 dB is considered. From Eq. (3.20) f is found to be 1.14, i.e., the maximum frequency of operation is 1.14 GHz. The crystal length and transducer radius are selected to be 4 mm and 100 μm , respectively, and the resulting lens illumination is shown in Fig. 3.19. This particular design results in approximately 3 dB of acoustic loss due to diffraction effects. The ZnO thickness should be 1.4 μm and the transducer electrode thicknesses are both selected to be 0.2 μm . These electrode thicknesses are less than 1/12 of a gold acoustic wavelength and will not

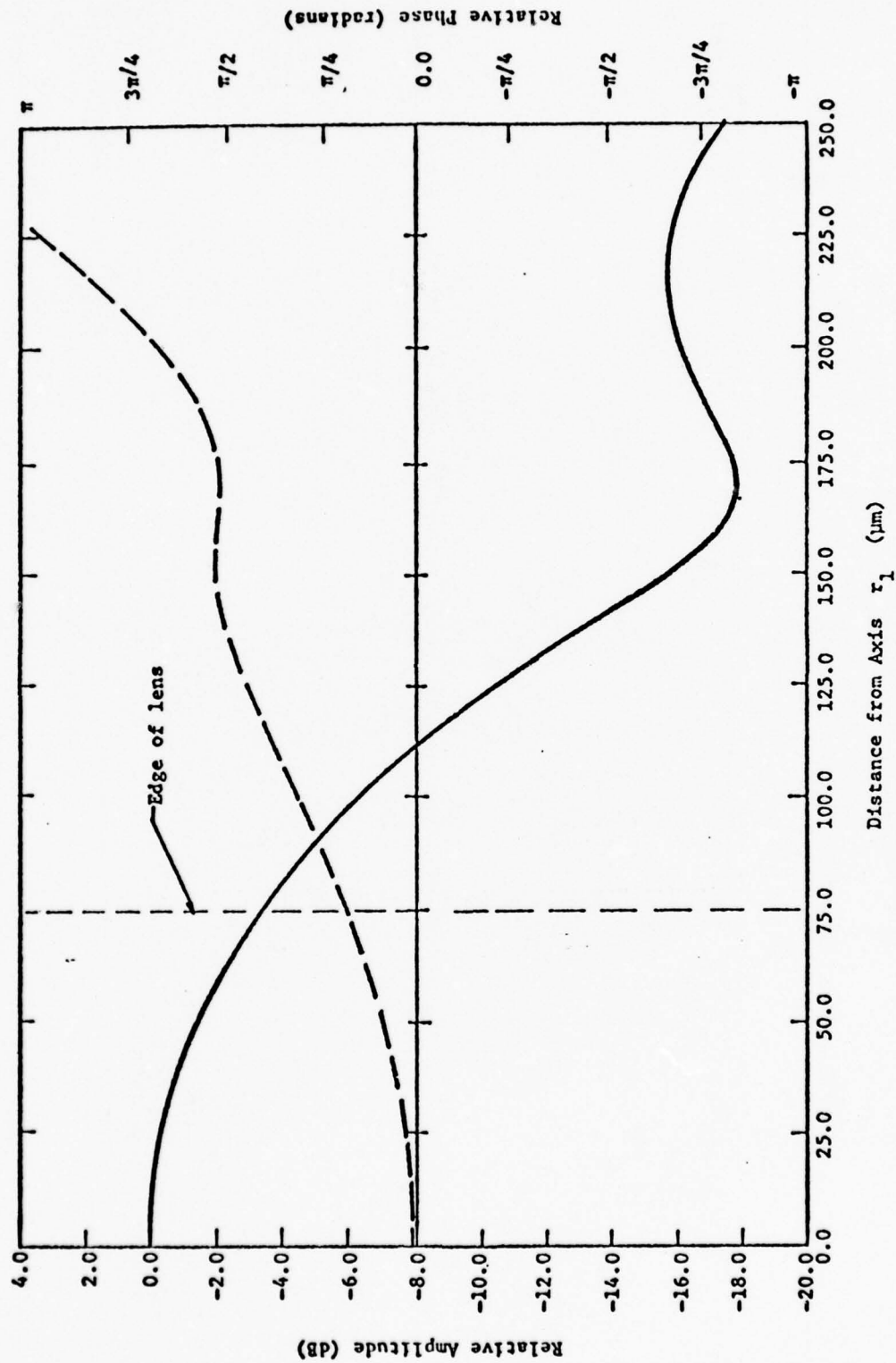


FIG. 3.19--Back focal plane illumination for 100 μm radius lens; $R_L = 100 \mu\text{m}$, $d = 4000 \mu\text{m}$, $\lambda = 10.0 \mu\text{m}$. The solid line is amplitude and the dashed line is phase.

significantly affect the transducer response. The glass thickness is chosen as 0.39 acoustic wavelengths which is $1.76 \mu\text{m}$ at this frequency. The resulting focal plane distribution for this lens is shown in Fig. 3.20.

As a second example consider a $40 \mu\text{m}$ lens that is to be operated at 60°C with a maximum loss of 70 dB in the water. From Fig. 2.11 the FM at this temperature is 1.44 and thus from Eq. (3.20) f is 2.8. Consequently the frequency of operation should be 2.8 GHz. Using the diffraction program of Appendix C the crystal length and transducer radius are selected as 2 mm and $50 \mu\text{m}$, respectively. The resulting lens illumination for this case is shown in Fig. 3.21. The transducer geometry is given by $t_0 = 0.6 \mu\text{m}$, $t_1 = 0.1 \mu\text{m}$ and $t_2 = 0.1 \mu\text{m}$. The theoretical response for this transducer structure was given in Fig. 3.11 where a matching network had already been included. The glass is again chosen to be 0.39 wavelengths or $0.72 \mu\text{m}$ for this frequency. The focal plane response for this lens is shown in Fig. 3.22.

From a comparison of Figs. 3.20 and 3.22 it can be seen that the focal plane response for both of these designs is quite similar. In both cases the 3 dB focal beam width is 0.65 acoustic wavelengths and thus it is expected that the resolution should be of the same order. If the glass thickness was chosen to be 0.25λ instead of 0.39λ for either of these designs, the resulting 3 dB beam width would be approximately 0.8λ . Thus, in conclusion, with the proper design of the transducer radius, crystal length and glass thickness it is possible to improve the resolving power of the acoustic lens by approximately 20% over what would be obtained from a straightforward design.

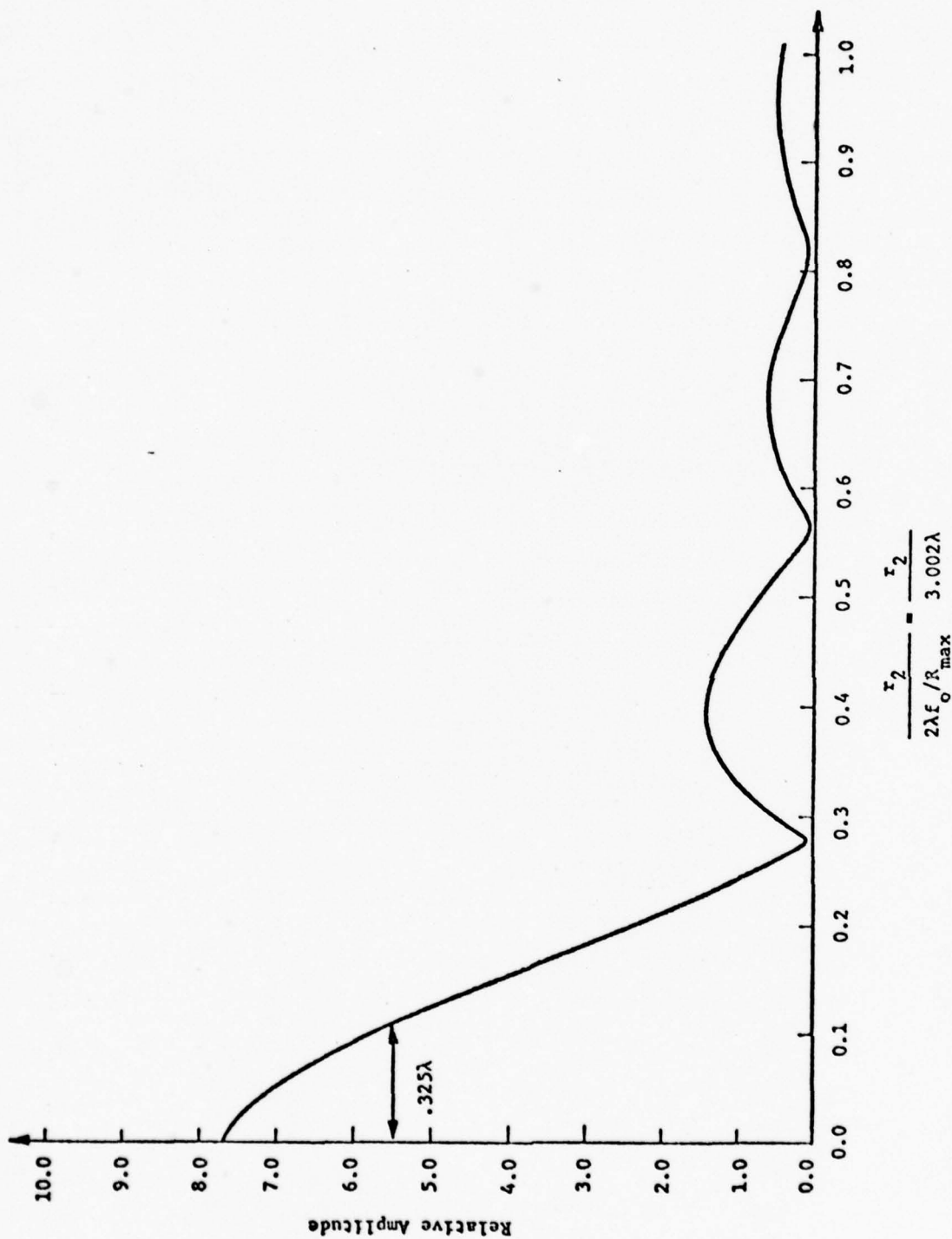


FIG. 3.20—Focal plane response for 100 μ m radius lens at 1.14 GHz. The 3 dB beamwidth is 0.85 μ m.

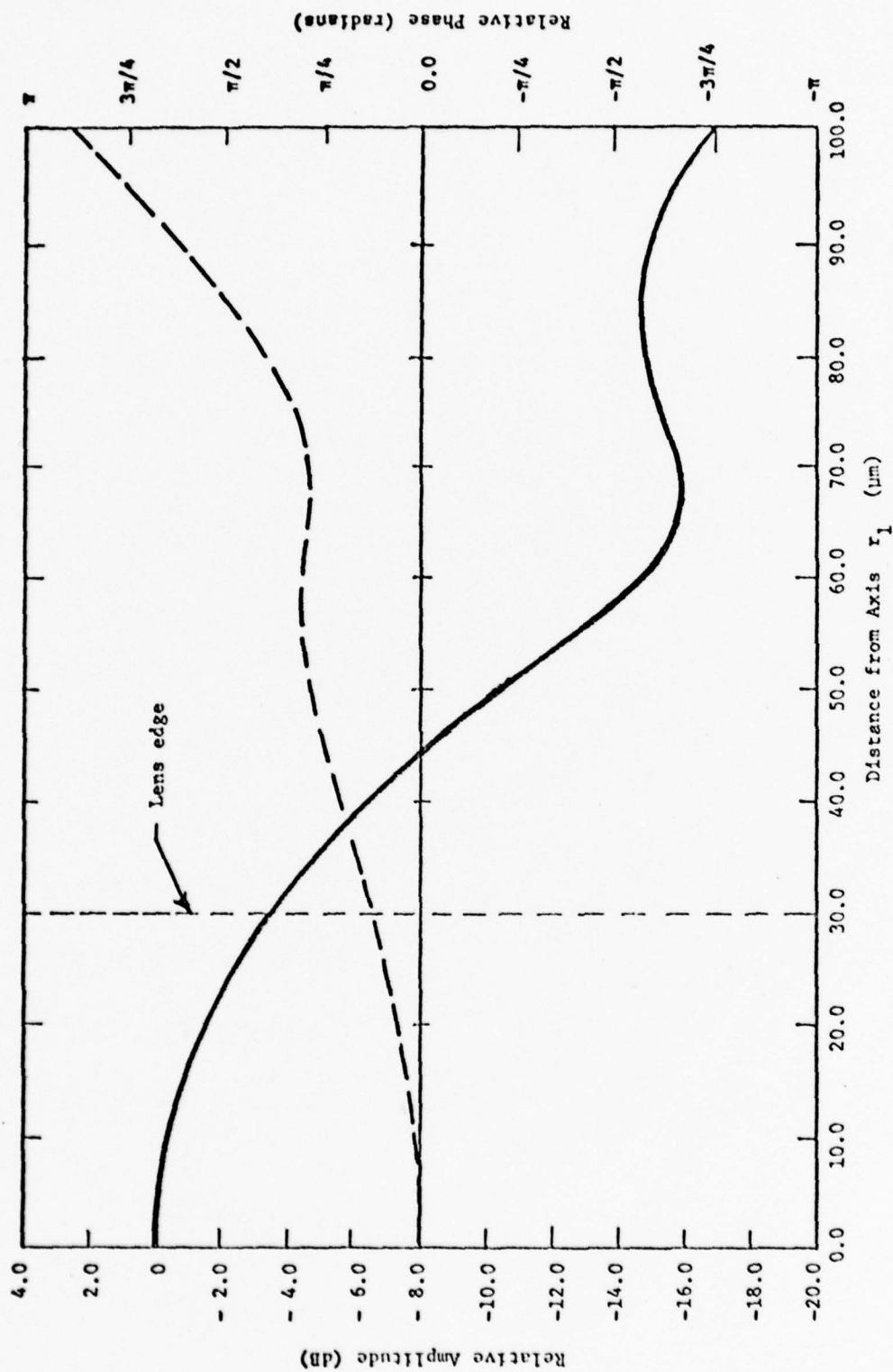


FIG. 3.21--Back focal plane illumination for $40 \mu\text{m}$ radius lens; $R_c = 50 \mu\text{m}$, $d = 2 \text{ mm}$, $\lambda = 4 \mu\text{m}$, $f = 2.8 \text{ GHz}$. The solid line is amplitude and the dashed line is phase.

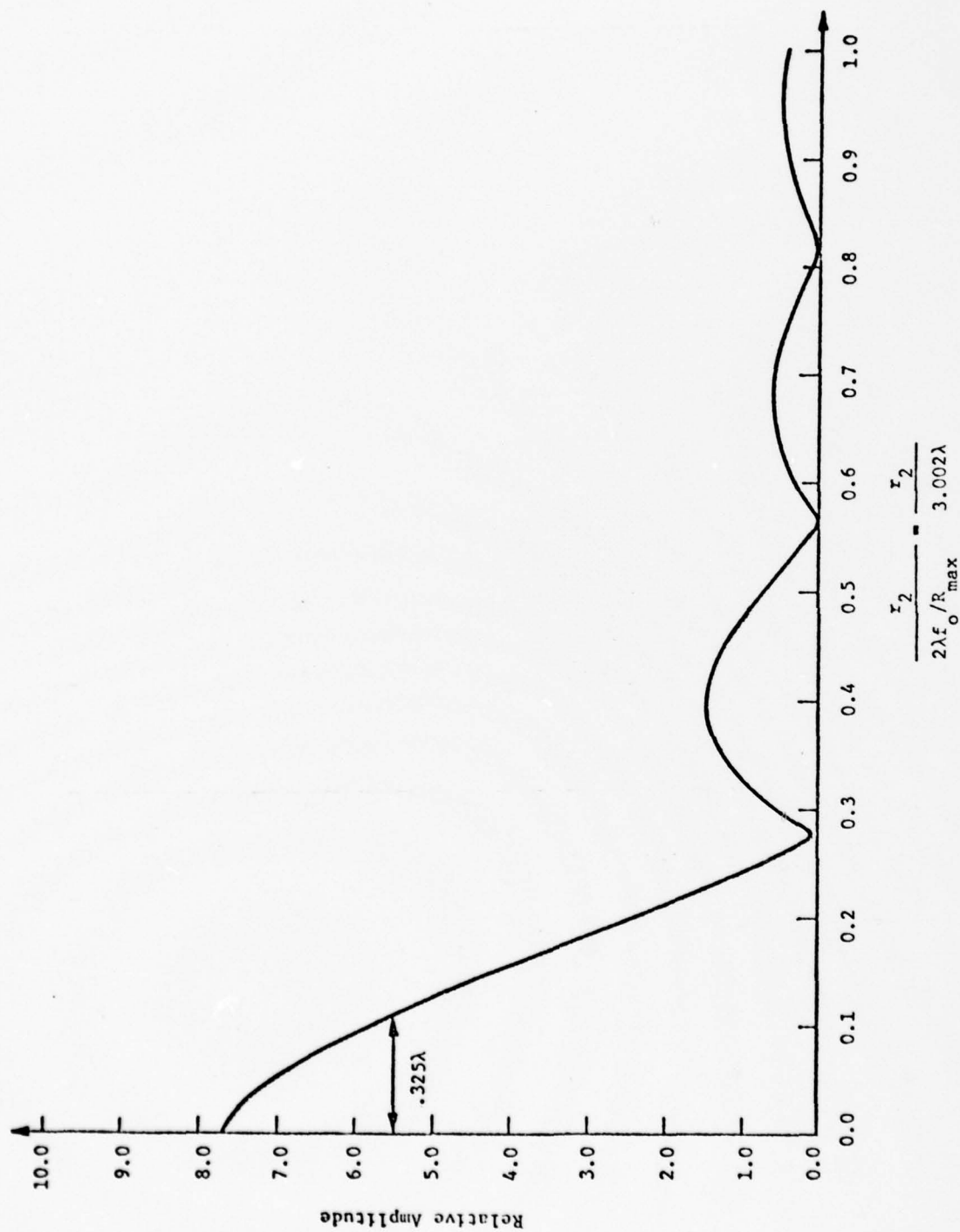


FIG. 3.22--Focal plane response for 40 μm radius lens at 2.8 GHz. The 3 dB beamwidth should be 0.36 μm .

REFERENCES — SECTION 3

- 3.1 J. Zemanek, "Beam Behavior Within the Nearfield of a Vibrating Piston," J. Acoust. Soc. Amer. 49, No. 1 (Part 2), pp. 181-191 (1971).
- 3.2 A. Atalar, "Acoustic Reflection Microscope," Ph.D. Dissertation, Stanford University (1978).
- 3.3 P. C. Waterman, "Orientation Dependence of Elastic Waves in Single Crystals," Phys. Rev. 113, No. 5, pp. 1240-1253 (1 March 1959).
- 3.4 E. P. Papadakis, "Diffraction of Ultrasound in Elastically Anisotropic NaCl and in Some Other Materials," J. Acoust. Soc. Amer. 35, No. 4, pp. 490-494 (April 1963).
- 3.5 E. P. Papadakis, "Diffraction of Ultrasound Radiating into an Elastically Anisotropic Medium," J. Acoust. Soc. Amer. 36, No. 3, pp. 414-422 (March 1964).
- 3.6 E. P. Papadakis, "Ultrasonic Diffraction Loss and Phase Change in Anisotropic Materials," J. Acoust. Soc. Amer. 40, No. 4, pp. 863-876 (1966).
- 3.7 T. M. Reeder and D. K. Winslow, "Characteristics of Microwave Acoustic Transducers for Volume Wave Excitation," IEEE Trans. on MTT, MTT-17, No. 11, pp. 927-941 (November 1969).
- 3.8 W. P. Mason, Electromechanical Transducers and Wave Filters, 2nd. ed. (Princeton, N.J.: Van Nostrand, 1948), pp. 195-209.
- 3.9 B. A. Auld, Acoustic Fields and Waves in Solids, Vol. 1 (John Wiley and Sons, New York, 1973), pp. 324-340.

- 3.10 E. K. Sittig, "Transmission Parameters of Thickness Driven Piezoelectric Transducers Arranged in Multi-Layer Configurations," IEEE Trans. on Sonics and Ultrasonics SU-14, pp. 167-174 (October 1967).
- 3.11 H. Seiki, A. Granato, and R. Truell, "Diffraction Effects in the Ultrasonic Field of a Piston Source and Their Importance in the Accurate Measurement of Attenuation," J. Acoust. Soc. Amer. 28, pp. 230-238 (March 1956).
- 3.12 M. T. Wauk II, "Attenuation in Microwave Acoustic Transducers and Resonators," Ph.D. Dissertation, Stanford University (1969).
- 3.13 S. Ramo, J. R. Whinnery, and T. Van Duzer, Fields and Waves in Communication Electronics (John Wiley and Sons, New York, 1965), pp. 27-33.
- 3.14 This chart was provided by R. C. Eggleton.
- 3.15 J. Heiserman, Private Communication.
- 3.16 K. C. Park and E. J. Weitzman, "E-Beam Evaporated Glass and MgO Layers for Gas Panel Fabrication," IBM J. of Res. and Dev., 22, No. 6 (November 1978), pp. 607-612.
- 3.17 L. M. Brekhovskikh, Waves in Layered Media (Academic Press, New York, 1960), pp. 15-36.
- 3.18 R. A. Lemons, "Acoustic Microscopy by Mechanical Scanning," Ph.D. Dissertation, Stanford University (1975).

4. Photoacoustics

Photoacoustics, or optoacoustics as is often known, is perhaps the most sensitive method for measuring optical absorption. In many instances the absorbed radiation is converted to heat and the thermal expansion that is associated with this heat gives rise to acoustic waves in the medium surrounding the absorbing region. The intensity of the optical beam is modulated at an appropriate frequency and the time response of the absorbing medium is such that the temperature of the heated region can follow the intensity variations of the optical beam. It is then the periodic variation in temperature that generates the acoustic waves. By varying the frequency of the optical wave it is possible to carry out spectroscopic measurements and use this to identify material properties. Much of the work has been done with modulating frequencies below 1 MHz. In the summer of 1978 we carried out an experiment which demonstrated that this technique could be adapted to the acoustic microscope.* We borrowed a pulsed laser and used it to heat deposited metallic films. The acoustic energy was detected with our lens at 800 MHz and the image was formed by mechanical scanning.

Since that time the work has been more or less dormant as we went through a planning stage. In other laboratories, however, the low frequency work on photoacoustic spectroscopy has been active. There is now a specialist conference at Iowa State in Ames in August and we were invited to present our work on photoacoustic imaging at that meeting.

In our laboratory at Stanford we have in this interval, demonstrated that the technique can be used to the SOS devices but heating the silicon epi-layers

*Applied Physics Letters 33, 923 (1 December 1978).

with the optical beam incident through the sapphire substrate. We feel that with a laser that is tunable through the bandgap of silicon and other semiconductors, we should be able to record some remarkable images.

During the interval covered by this report and in preparation for the Iowa State Conference, we have worked on the theory of photoacoustic conversion of energy from optical to acoustic with heat as the intermediate step and this work will soon be complete. We are particularly concerned with heat generated in solid materials and the propagation through layers to the liquid interface with the lens of the acoustic microscope. Heretofore, we have used pulsed lasers to achieve the modulation of the heating but this is inefficient since the acoustic energy is not confined to a single frequency. To remedy this we are constructing an optical modulator to cover the range of 10 - 1000 MHz. We will be using a design suggested by Ivan Kaminow of Bell Laboratories. This modulator will allow us to lock the modulating frequency with that of the acoustic receiver and increase the sensitivity of the overall instrument.

5. Imaging with High Velocity Liquid Metals - Gallium

In the last semiannual report we discussed a system where we used liquid gallium in the acoustic cell in place of water. This made it possible to focus the acoustic beam inside of a solid with a diffracted limited waist. Jipson^{5.1,5.2} has pointed out that this can be accomplished if we convert from longitudinal waves in the gallium to shear waves in the solid. For many solids the shear wave velocity is less than the longitudinal wave velocity in gallium and it is this factor that permits us to reduce the aberrations. The nature of these aberrations was discussed in our last semiannual report and some calculations were carried out for a gallium-steel interface. Since that time we have performed similar calculations for a gallium fused quartz interface and these results will be included here. We have also obtained experimental results that demonstrate proper focusing of shear waves with acoustic waves at 1 GHz after they have traveled through 75 μm of fused quartz.

The significance of these results - as pointed out in the introduction - is as follows. The velocity of shear waves in solids is not much greater than the velocity of longitudinal waves in liquids ($v_{\text{sh}} = 2 \times 10^5$ cm/sec in fused quartz as compared to $v_{\text{long}} = 1.5 \times 10^5$ cm/sec in water). Therefore the wavelength and the diameter of the waist of a focused beam are similar for the two cases. However, the absorption coefficient for sound in gallium

^{5.1}V.B. Jipson, "Acoustic Microscopy of Interior Planes," (May 1979); to appear in Applied Physics Letters.

^{5.2}V.B. Jipson, "Acoustic Microscopy at Optical Wavelengths," Ginzton Laboratory Report No. 2980 (June 1979).

is an order of magnitude less than it is for water. We can therefore work at much higher frequencies with the liquid metal system and it is not inconceivable that the resolving power will one day exceed the value that we have reached with water.

Before we present the experimental results we want to discuss the process of conversion from longitudinal to shear waves at the liquid-solid interface. Keep in mind that we are dealing with spherically converging waves typical of the acoustic beam in acoustic microscopes.

In order to calculate the internal focusing properties of the acoustic microscope, it is necessary to understand how longitudinal and shear waves are excited within the solid when a longitudinal wave is incident at the surface. This problem is readily solved by applying the acoustic boundary conditions (continuity of normal stress and particle displacement and zero tangential stress at the solid surface) to the liquid-solid interface. The results for the reflection and transmission coefficients are:^{5.3}

$$R_L = \frac{Z_1 \cos^2 2\phi'_s + Z_t \sin^2 2\phi'_s - Z}{Z_1 \cos^2 2\phi'_s + Z_t \sin^2 2\phi'_s + Z}$$

$$T_L = \frac{\rho}{\rho_1} \frac{2 Z_1 \cos 2\phi'_s}{Z_1 \cos^2 2\phi'_s + Z_t \sin^2 2\phi'_s + Z}$$

$$T_s = - \frac{\rho}{\rho_1} \frac{2 Z_t \sin 2\phi'_s}{Z_1 \cos^2 2\phi'_s + Z_t \sin^2 2\phi'_s + Z}$$

^{5.3} L.M. Brekhovskikh, Waves in Layered Media (Academic Press, New York, 1960), pp. 15-36

where

$$Z = \frac{\rho_2 V_2}{\cos \phi}, \quad Z_L = \frac{\rho_3 V_{3L}}{\cos \phi'_L}, \quad Z_t = \frac{\rho_3 V_{3s}}{\cos \phi'_s},$$

ρ_2 is the liquid density, V_2 is the acoustic velocity in the liquid, ρ_3 is the solid density, V_{3L} is the longitudinal acoustic velocity in the solid, V_{3s} is the shear acoustic velocity in the solid, R_L is the amplitude of the reflected longitudinal wave (assuming the incoming wave was unit amplitude), T_L is the amplitude of the transmitted longitudinal wave, T_s is the amplitude of the transmitted shear wave and from Snell's law

$$\frac{V_2}{\sin \phi} = \frac{V_{3L}}{\sin \phi'_L} = \frac{V_{3s}}{\sin \phi'_s},$$

where ϕ is the angle of incidence, ϕ'_L is the angle of refraction for the longitudinal wave and ϕ'_s is the angle of refraction for the shear wave.

If we are to calculate the energy transfer across the boundary, we must know the partition of acoustic energy into the various components. Conservation of energy at the boundary requires

$$RL + TL + TS = 100\%$$

where $RL = 100 R_L^2$ is the percent of reflected longitudinal energy, $TL = 100 (Z/Z_L) (\rho_1/\rho)^2 T_L^2$ is the percent of transmitted longitudinal energy and $TS = 100 (Z/Z_t) (\rho_1/\rho)^2 T_s^2$ is the percent of transmitted

shear energy.^{5.3} In Fig. 5.3 the partition of acoustic energy as a function of ϕ' is shown for a water-fused quartz and gallium-fused quartz interface. It can be seen for the water-fused quartz boundary that more than 60% of the incident energy is reflected as a longitudinal wave. At low angles of refraction approximately 30% is transmitted as a longitudinal wave and above the longitudinal critical angle ($\phi = 15^\circ$) up to 40% is transmitted as a shear wave. For the gallium-fused quartz case the situation is quite different. For low angles of incidence nearly 100% of the energy is transmitted as a longitudinal wave and above the longitudinal critical angle ($\phi = 29.7^\circ$) almost 100% is converted into a transmitted shear wave.

The acoustic lens generates an angular spectrum of plane waves that impinge on the object with a maximum angle of incidence ϕ that is approximately 20% less than the maximum opening angle of the lens. It is obvious from Fig. 5.3 that; 1) the use of gallium in place of water results in significantly improved energy transfer across the boundary, and 2) shear waves can be efficiently excited if the maximum angle of incidence exceeds the longitudinal critical angle.

The acoustic transfer functions for the longitudinal ($T_L(\theta)$) and shear ($T_s(\theta)$) waves are utilized in the next section where the acoustic field distribution inside the object is calculated.

Acoustic Field Within the Object

A measure of the imaging potential inside materials with this technique can be obtained by considering the geometric aberrations of Eq. (5.1). A more rigorous approach would include the calculation of the acoustic field

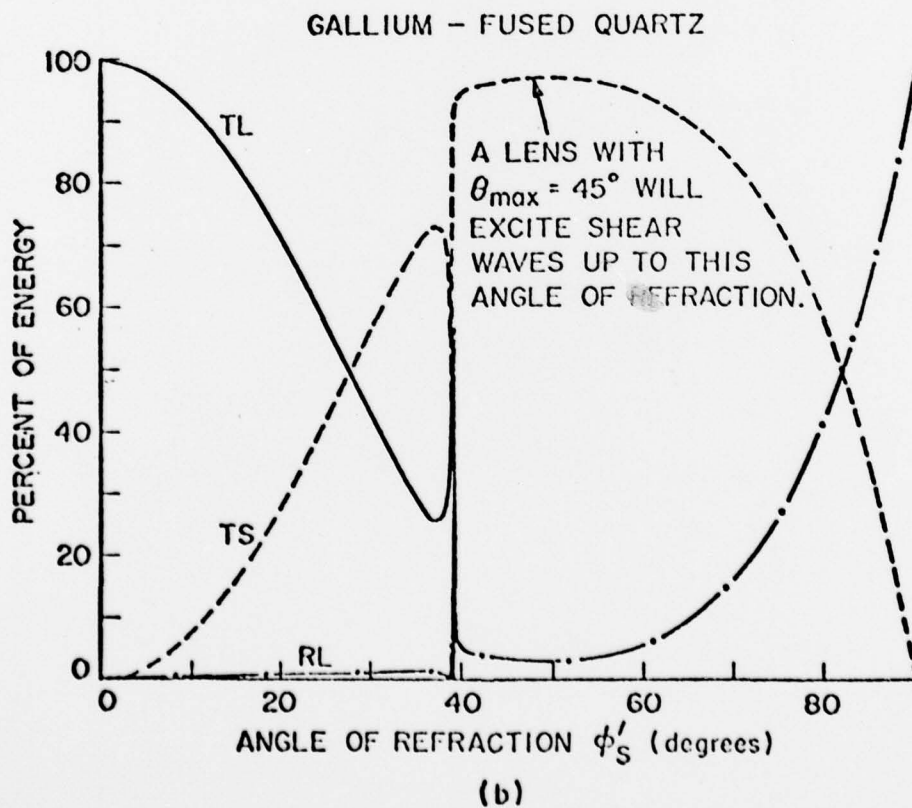
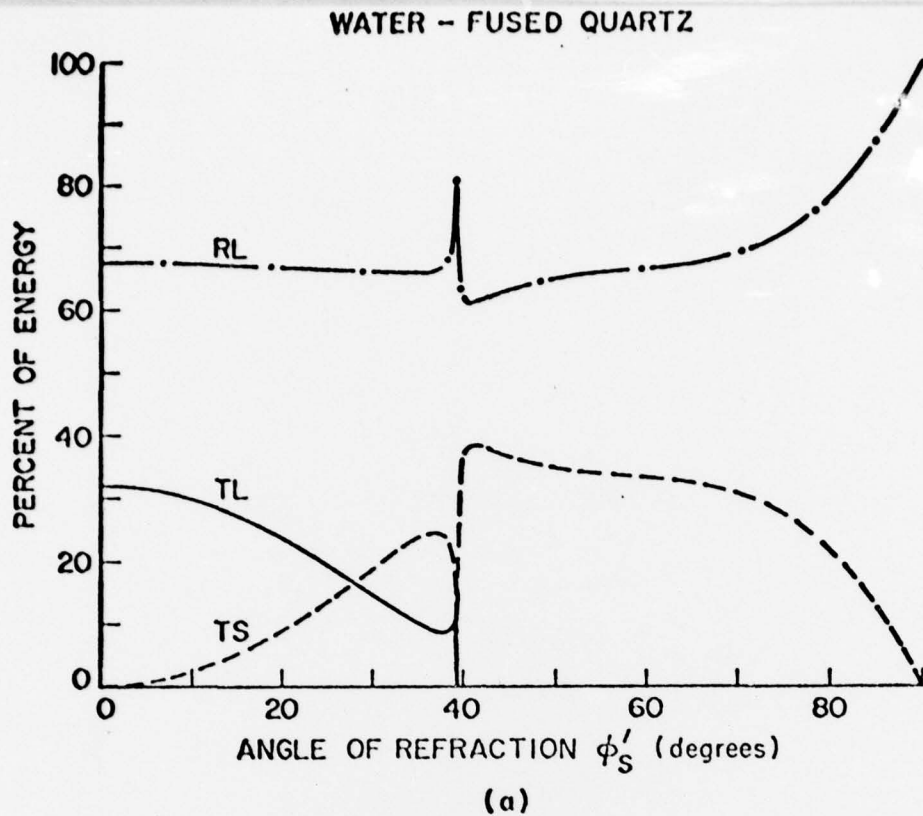


FIG. 5.3--Partition of acoustic energy at a water-fused quartz and a gallium-fused quartz interface.

distribution inside the object as a function of depth. This is accomplished by using an angular spectrum approach as outlined below.

The geometry for this calculation is shown in Fig. 5.4. Assume the back focal plane distribution of the acoustic lens (Plane 1) is given by $U_1(r_1)$ and the effective pupil function is given by;

$$P_e(r_1) = P(r_1) \frac{\cos \theta'}{\cos \theta}$$

where $P(r_1)$ is the generalized pupil function for the lens. The focal plane distribution (Plane 2) without the object present is given by;^{5.4,5.5}

$$U_2(r_2) = \exp\left\{jk_\ell r_2^2/2f_o\right\} \mathcal{H}\left\{P_e(r_1)U_1(r_1)\right\}_{\rho=r_2/\lambda_\ell f_o} \quad (5.2)$$

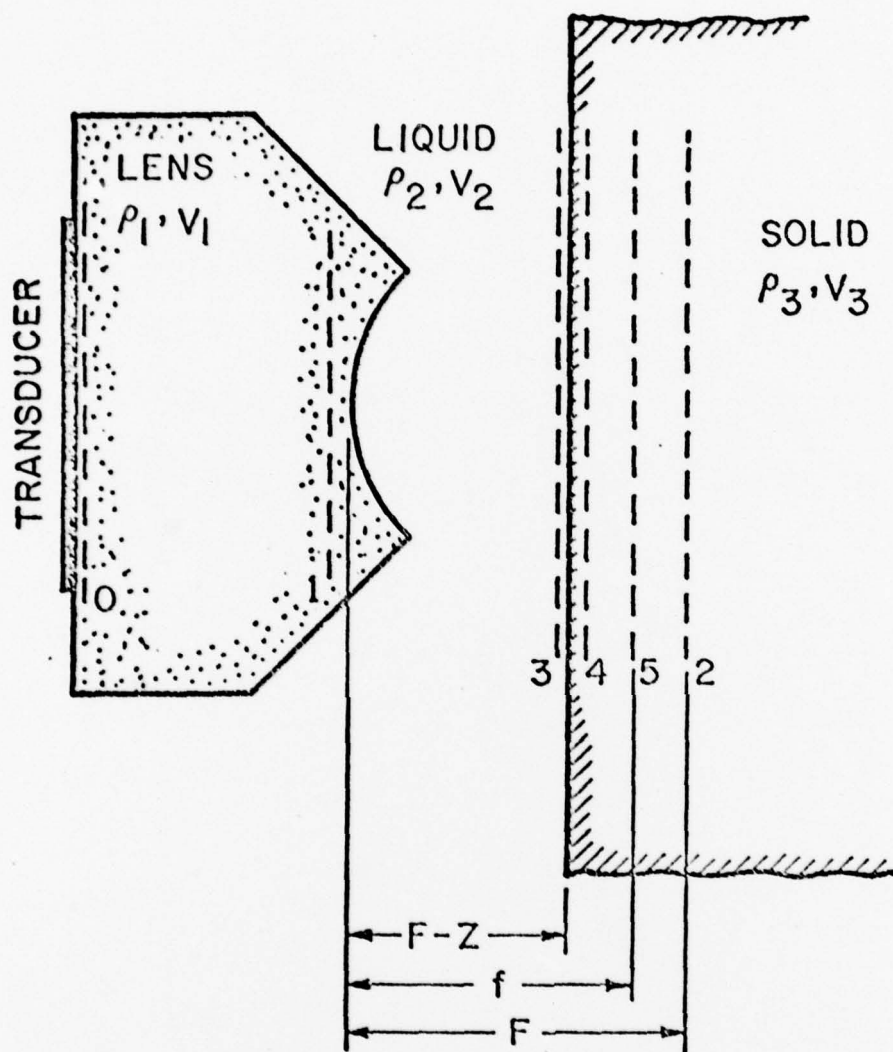
where $k_\ell = 2\pi/\lambda_\ell$, λ_ℓ is the acoustic wavelength in the liquid, f_o is the focal length of the lens and $\mathcal{H}\{P_e(r_1)U_1(r_1)\}_{\rho=r_2/\lambda_\ell f_o}$ stands for the zero-order Hankel transform or angular spectrum of the quantity in brackets with the spatial frequency ρ evaluated at $r_2/\lambda_\ell f_o$. At the focal plane r_2 is only significant over a radius of a few wavelengths and thus to a good approximation the exponential can be ignored. The angular spectrum^(5.6) at the focal plane can thus be written as:

$$U_2(\rho) = \mathcal{H}\left\{U_2(r_2)\right\} \approx P_e(\lambda\rho f_o)U_1(\lambda\rho f_o) . \quad (5.3)$$

In order to calculate the acoustic field distribution within the object, the angular spectrum must first be propagated to Plane 3 of Fig. 5.4,

^{5.4} R.A. Lemons, "Acoustic Microscopy by Mechanical Scanning," Ph.D. Dissertation, Stanford University (1975).

^{5.5} H.K. Wickramasinghe, J. Appl. Phys. 50 (12), 664 (1979).



F = LENS FOCAL LENGTH

f = FOCAL LENGTH INSIDE SOLID

Z = DISTANCE OBJECT MOVED FROM FOCAL PLANE

FIG. 5.4--Geometry for the calculation of the acoustic field at planes inside the object.

i.e., a plane just inside of where the object will be positioned. At Plane 3 the angular spectrum is:

$$U_3(\rho) = U_2(\rho) \exp \left\{ (\alpha_\ell - jk_\ell) \sqrt{1 - (\rho\lambda_\ell)^2} z \right\} \quad (5.4)$$

where α_ℓ is the attenuation coefficient in the liquid and the exponential factor accounts for the propagation of the various angular components.^(5.5-5.6) The acoustic field distribution at Plane 3 could now be calculated by taking the Hankel transform of $U_3(\rho)$. This is the technique that was utilized in Chapters 2 and 3 to find the "focal plane" distribution for the acoustic lens in the presence of phase errors due to acoustic matching layers and lens aberrations. However, it is the acoustic field distribution within the object that concerns us here. At this point the object can be inserted and the angular spectrum at Plane 4 (a plane infinitesimally removed from Plane 3 but across the liquid-solid interface) can be obtained through multiplication of the spectrum at Plane 3 by the appropriate acoustic transfer function for the liquid-solid interface, $T(\rho)$, as described in the previous section. The spectrum can then be propagated within the solid to the plane of interest (Plane 5) by multiplying each angular component by the appropriate phase term, i.e.,

$$U_5(\rho) = U_3(\rho) T(\rho) \exp \left\{ (jk_s - \alpha_s) \sqrt{1 - (\rho\lambda_s)^2} z \right\} \quad (5.5)$$

where $k_s = 2\pi/\lambda_s$, λ_s is the appropriate wavelength in the solid and

^{5.6} J.W. Goodman, Introduction to Fourier Optics (McGraw-Hill, New York, 1968), p. 48.

α_s is the corresponding acoustic attenuation coefficient. The acoustic field distribution is then found by taking the zero-order Hankel transform, i.e.,

$$U_5(r_5) = \mathcal{H}\{U_5(\rho)\} \quad (5.6)$$

A computer program was written to perform the above operations and also to calculate the effective pupil function for the lens.

In Fig. 5.5, calculated acoustic field distributions are shown for a gallium-fused quartz geometry. The calculations are based on the following assumptions: 1) $R = 200 \mu\text{m}$, 2) $\theta_{\text{max}} = 45^\circ$, 3) $f = 1.0 \text{ GHz}$, 4) $\alpha_g/f^2 = 1.58 \times 10^{-17} \text{ sec}^2/\text{cm}$, and 5) $\alpha'_s/f^2 = 0. \text{ sec}^2/\text{cm}$. In Fig. 5.5(b) results are shown for the longitudinal wave case at depths of 70, 75 and 80 μm within the material after the object has been translated (in theory) 190 μm inside the focal plane. It can be seen for this case that the best focus occurs at a depth of 75 μm . The paraxial focal depth for this geometry is 91 μm which is 20% larger than the calculated focal depth. It is not surprising that the best focus occurs at a plane considerably in front of the paraxial focal plane since the geometric aberrations for this case will be severe. The 3 dB acoustic beamwidth is $0.76 \lambda_{3L}$ which is 4.54 μm at 1 GHz. It is somewhat surprising that the beamwidth is this narrow considering the large aberration effects for this case, but these effects are compensated somewhat by the fact that the effective lens F-number for this geometry is 0.5. The low F-number arises from the fact that acoustic energy is

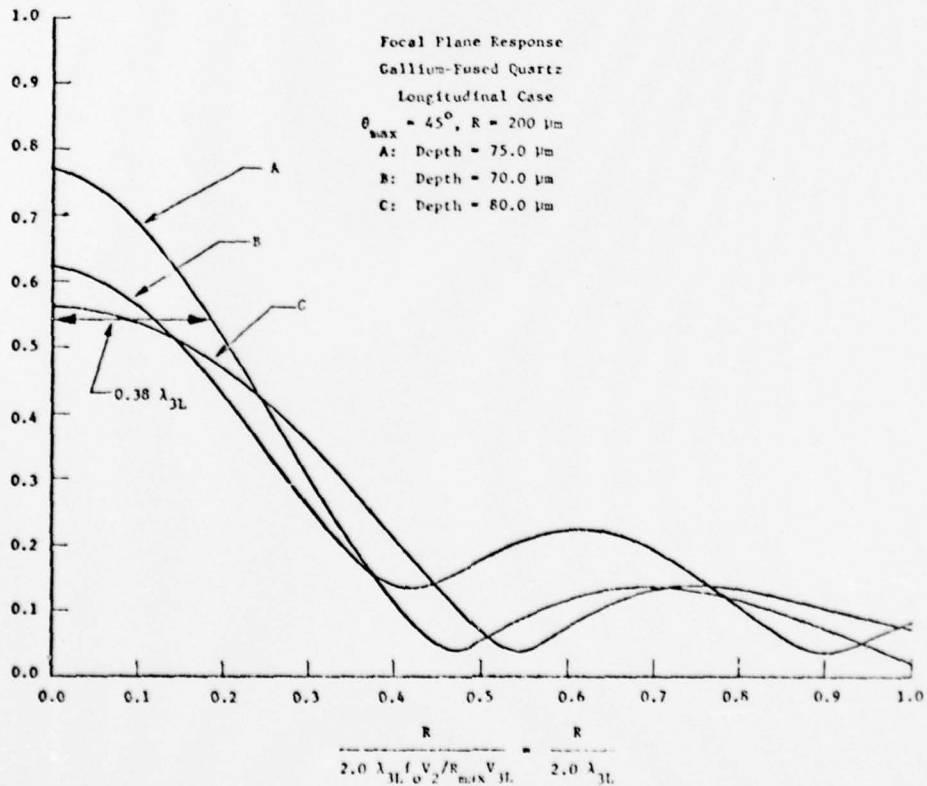
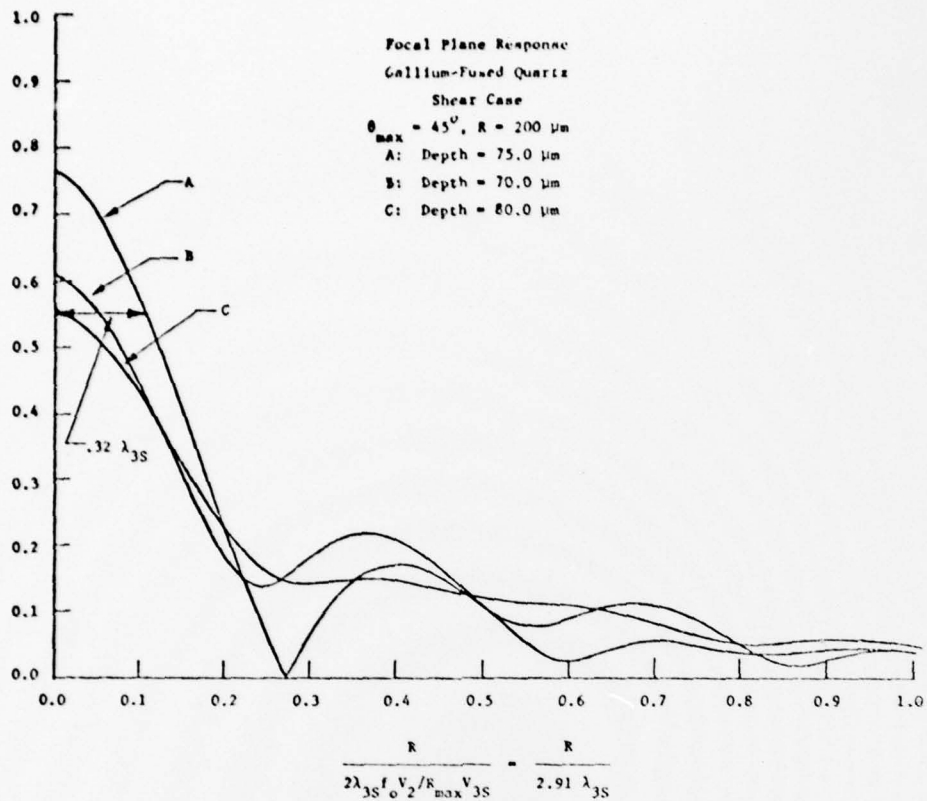


FIG. 5.5--Acoustic field amplitude at different depths for both the (a) shear and (b) longitudinal wave case.

incident on the object at angles up to the longitudinal critical angle. In fact some of the incident energy is above the critical angle and thus $T(\rho) = 0.0$ for these components. In Fig. 5.5(a) similar results are shown for the shear wave case. The value of Z was assumed to be $105 \mu\text{m}$. The corresponding paraxial focal plane for this geometry is $80.9 \mu\text{m}$ which is 6.8% greater than the calculated focal plane of $75.0 \mu\text{m}$. The 3 dB focal width is $0.64 \lambda_{3s}$ which is $2.4 \mu\text{m}$ at 1.0 GHz, nearly a factor of two less than for the longitudinal case.

From these calculations it can be concluded that the use of shear waves within the material for imaging purposes can result in substantially improved resolution. This is true for the case discussed here even though the effective F-number for the lens in the shear wave case is 40% larger than for the longitudinal wave case.

III. ADDITIONAL ACTIVITIES

A. A number of talks was given during this interval which attracted a good deal of interest in this field.

1. Seminar for the Petroleum Consortium as organized by Prof. A. Nur.
2. Invited talk: American Physics Society of Chicago, March 19th. As a result of this our work was written up in Physics Today, page 20, May 1979.
3. Seminar for the Department of Material Science at Stanford.
4. Invited talk at Bell Laboratory, "Kempfner Memorial Lecture," May 1979.
5. Invited talk: Acoustical Society of America, Boston, June 1979.
6. Participated in the ARP/AF Review in Quantitative NDE at LaJolla in July. One invited talk and a poster session.

B. The following list of visitors toured our laboratory during this interval.

1. B. Heidenreich and D. Kelth - Bell Labs.
2. Brian Shubert - Honeywell in Denver.
3. W. Bruitman - Bell Labs.
4. Bill Ham - RCA - Princeton
5. Bill Livesay - Georgia Tech
6. Jim McGroddy - IBM - Yorktown
7. Jim Kurtzig - Hewlett Packard Labs
8. Don Chamberlain - FMC
9. Bob Dynes - Bell Labs

10. Kuma Patel - Bell Labs
11. E. Nishimma - Nekkei Electronics
12. B. McDonald - Intel
13. W. Webster - RCA Princeton
14. R. Von Guffeld - IBM - Yorktown
15. R. Scruby - Harmell - England
16. R. Scouten and B. Gethner - Exxon Labs
17. Larry Kessler - Sonorscan
18. Dave Bishop - Bell Labs.
19. Larry Cummings - Wright-Paterson
20. MacFulwyler - Becton - Dickenson